Table des matières

I Astroparticles **3**

Kael HANSON : ***Particle Astrophysics*** **5**
1.1 Introduction . . . 5

Hélène LAFFON : ***Etude des sources gamma dans le plan galactique avec H.E.S.S.*** **7**
2.1 Introduction . . . 7
2.2 Préambule . . . 7
2.3 L'instrumentation Čerenkov . . . 8
2.4 Amélioration de la résolution angulaire . . . 9
2.5 Etude d'un reste de supernova : G22.7-0.2 . . . 9
2.6 Conclusion . . . 10

Karim Louedec : ***Extracting Aerosol properties by the Central Laser Facility at the Pierre Auger Observatory*** **13**
3.1 Introduction . . . 13
3.2 The Central Laser Facility . . . 14
3.3 Extracting of the Aerosol Phase Function . . . 14

Moritz Münchmeyer : ***Search for large-scale anisotropies in the distribution of cosmic rays with the Pierre Auger Observatory*** **19**
4.1 Introduction . . . 19
4.2 The Pierre Auger Observatory . . . 19
4.3 1-dimensional large-scale anisotropy search . . . 19
4.4 2-dimensional large-scale anisotropy search . . . 21

Michal Was : ***Searching for gravitational waves associated with gamma-ray bursts*** **23**
5.1 Gravitational waves . . . 23
5.2 Gravitational wave detectors . . . 23
5.3 Gamma-ray bursts . . . 24
5.4 Data analysis . . . 24
5.5 Results . . . 25

Charif, Ziad : ***Indirect Search for Dark Matter with the ANTARES Neutrino Telescope*** **27**
6.1 Introduction . . . 27
6.2 Dark Matter . . . 27
6.3 The ANTARES Neutrino Telescope . . . 28
6.4 Indirect search of Dark Matter with ANTARES . . . 29
6.5 Conclusions . . . 30

A. Rebai : ***Estimation de rayon de courbure des gerbes atmosphériques par la méthode de radio-détection avec CODALEMA*** **31**
7.1 Introduction . . . 31
7.2 Principe de la reconstruction du centre d'émission radio . . . 31
7.3 Résultat de reconstruction du centre d'émission radio . . . 32
7.4 Conclusion . . . 33

Première partie

Particle Astrophysics



François
RABELAIS



Rabelais
FRANÇOIS

Particle Astrophysics

Kael HANSON

Université Libre de Bruxelles - IIHE, Bruxelles, Belgium



Résumé

1.1 Introduction

Astronomy's messenger particles have been since the beginning optical photons : they easily reach our eyes and our telescopes from great distances and point back to their origins. As as result we have learned a great deal about the Universe from these particles alone. In the past 50 years, the electromagnetic spectrum was broadened with the introduction of radio, IR, and UV astronomy. More recently, medium and high-energy gamma rays have been used as messengers : gamma ray astronomy is coming of age and revealing many things about the non-thermal universe and associated high-energy phenomena. Particle astrophysicists are looking to other particles, the neutrinos, to obtain more information on these phenomena deep within the objects and very close to central engines, and hope that the neutrinos can answer a standing, fundamental question : what is the origin of the observed cosmic ray spectrum, extending all the way to 10^{20} eV ? It is believed that these cosmic super-accelerators which supply the extreme end of the spectrum cannot be supernova remnants which appear to be the perfect candidates for the lower and moderate energy cosmic rays. However, even this still remains to be verified [1]

Particle astrophysics is in fact a broad field. ASPERA, the European network for coordinating research in this domain has laid down seven questions central to the mission of the field [2]. They are :

- What is the Universe made of ? In particular : What is dark matter ?
- Do protons have a finite lifetime ?
- What are the properties of neutrinos ? What is their role in cosmic evolution ?
- What do neutrinos tell us about the interior of the Sun and the Earth, and about supernova explosions
- What is the origin of cosmic rays ? What is the view of the sky at extreme energies ?
- What will gravitational waves tell us about violent cosmic processes and about the nature of gravity ?

The program of talks presented at this meeting of the Journées de Jeunes Chercheurs reflects the diversity of the field with presentations from young researchers working on experiments in the the gamma-ray (HESS), gravitational wave (LIGO/Virgo), ultrahigh-energy cosmic ray (Pierre Auger and CODALEMMA), and neutrino telescope (ANTARES) communities.

Références

[1] J.Blümer, R.Engel, and J.Hörandel. Cosmic Rays from the Knee to the Highest Energies. arXiv.org :0904.0725

[2] ASPERA Roadmap (`http://www.aspera-eu.org/images/stories/roadmap/aspera_roadmap.pdf`)

Etude des sources gamma dans le plan galactique avec H.E.S.S.



Hélène LAFFON
Laboratoire Leprince-Ringuet, Palaiseau

Résumé

L'étude du rayonnement gamma observé dans le plan galactique permet d'en apprendre davantage sur les caractéristiques des restes de supernovae et des nébuleuses à vent de pulsar. Cela peut aussi confirmer l'origine galactique d'une partie des mystérieux rayons cosmiques. Nous décrivons ici les différents processus d'accélération et d'émission à l'oeuvre dans ces objets, ainsi que les techniques de détection et d'analyse du rayonnement gamma à l'aide de télescopes à effet Čerenkov.

2.1 Introduction

A l'origine, l'astronomie gamma a pour but de sonder indirectement l'origine du rayonnement cosmique afin de comprendre où et comment les rayons cosmiques sont accélérés. Depuis une vingtaine d'années, l'instrumentation et les techniques de détection des observatoires Čerenkov ont fait des progrès considérables, et le nombre de sources gamma découvertes est passé de 10 en 2004 à 120 en 2010. Parmi ces sources, près des deux tiers sont galactiques, et pourraient expliquer l'origine des rayons cosmiques observés jusqu'à 10^{15} eV. Dans ce proceeding, nous passerons tout d'abord en revue quelques types de sources observables dans notre galaxie, puis nous décrirons les principaux mécanismes d'accélération des particules chargées ainsi que les processus d'émission en rayons gamma. Par la suite, nous expliquerons le principe de l'instrumentation Čerenkov et les méthodes d'analyse. Enfin, nous justifierons la nécessité d'améliorer la résolution angulaire et nous étudierons l'émission gamma observée sur un reste de supernova.

2.2 Préambule

2.2.1 Quelques sources galactiques

Au sein de notre galaxie, différents types d'objets constituent de potentiels accélérateurs de particules non thermiques. Les principales sources sur lesquelles nous nous focaliserons ici sont :

-Les restes de supernovae (SNR) : Lors de l'explosion d'une supernova, le plasma chaud de l'étoile est éjecté et va former une onde de choc avec le mileu interstellaire. Les particules chargées vont ensuite pouvoir être accélérées dans cette onde de choc. Selon les modèles théoriques, environ 10% de l'énergie initiale de la supernova serait disponible pour accélérer les rayons cosmiques. Ces objets ont généralement une morphologie en coquille observée en ondes radio, due à l'émission synchrotron des électrons accélérés dans l'onde de choc. En rayons gamma, ils peuvent présenter des morphologies diverses, dépendant de la répartition du milieu interstellaire environnant.

-Les pulsars et leurs nébuleuses : L'explosion d'une supernova conduit généralement à la création d'un objet compact, résidu de l'étoile mère. Les pulsars sont des étoiles à neutrons en rotation rapide et présentant un très fort champ magnétique. Lorsque des particules chargées sont arrachées à la surface du pulsar, un vent de pulsar est créé et va "remplir" la nébuleuse, conduisant à une émission gamma observée à l'intérieur du reste de supernova.

-Les nuages moléculaires : Composés d'hydrogène ou de molécules plus complexes comme le ^{13}CO, ces objets ne sont pas des accélérateurs de particules chargées, mais leur cible. En effet, l'interaction des rayons cosmiques avec les molécules des nuages donne lieu à des processus hadroniques produisant des rayons gamma.

2.2.2 L'accélération de Fermi

Fermi 2^{eme} ordre :

L'accélération de particules chargées nécessite un champ électrique non nul, or le milieu interstellaire est globalement neutre. Cependant, en 1949, Fermi propose la théorie suivante [1] : lorsque les particules chargées entrent en collision avec des nuages magnétisés, celles-ci peuvent gagner de l'énergie petit à petit en multipliant les collisions frontales (dont la probabilité est légèrement plus grande que celle des collisions fuyantes) sur les inhomogénéités magnétiques. Le gain moyen en énergie correspondant est de : $< \frac{\Delta E}{E} > \sim \frac{4}{3}\beta^2$, où $\beta = v/c$ et v est la vitesse du nuage magnétisé.

Fermi 1^{er} ordre :

Ce mécanisme concerne quant à lui l'accélération par onde de choc, qui a lieu dans les restes de supernovae. Les particules traversent plusieurs fois le choc, en gagnant de l'énergie à chaque collision, et dans ce cas le gain moyen en énergie est du premier ordre : $< \frac{\Delta E}{E} > \sim \frac{4}{3}\beta$. Ce processus est donc beaucoup plus efficace que le précédent.

Ces deux processus conduisent à un spectre en loi de puissance, en accord avec le spectre observé des rayons cosmiques.

2.2.3 Processus d'émission gamma

Le spectre d'émission observé va dépendre de la nature des particules chargées (électrons/positrons ou hadrons).

Les processus leptoniques :

En présence d'un champ magnétique, les particules vont émettre un rayonnement synchrotron, observable de la radio au MeV. Elles sont aussi soumises au rayonnement de freinage (ou Bremsstrahlung) en présence de noyaux cibles dans les milieux environnants. De plus, elles vont intéragir par processus "Compton inverse" avec les photons diffus présents dans le milieu interstellaire (fond diffus cosmologique, fond infrarouge dû aux poussières, ou tout simplement la lumière des étoiles en optique) et propulser ces photons en rayons gammas en leur transmettant leur énergie. Enfin, le processus appelé "Synchro-Self Compton" consiste en une combinaison entre le rayonnement synchrotron et le "Compton inverse" : les leptons vont transmettre leur énergie aux photons du rayonnement synchrotron, les propulsant en rayons gammas.

Les processus hadroniques :

Dans le cas hadronique, le principal processus à l'oeuvre a lieu en présence de nuages moléculaires, composés également de hadrons, mais peu énergétiques. Les rayons cosmiques vont alors intéragir avec les particules du nuages et produire des pions neutres, qui se désintègrent ensuite en gammas : $pp \rightarrow \pi_0 \rightarrow \gamma\gamma$.

Les modèles théoriques tenant compte des caractéristiques du milieu étudié (densité du rayonnement diffus ou des nuages moléculaires par exemple) prédisent le spectre observé dans toute la gamme de longueurs d'onde dans les cas leptoniques et hadroniques. La confrontation des observations réalisées par divers instruments à différentes longueurs d'onde avec ces modèles peut ensuite permettre de trancher entre les deux types de processus et de remonter à la nature des particules primaires. Cependant, cette distinction s'avère généralement difficile car des modèles hybrides complexes sont aussi possibles, et souvent plus vraisemblables que les modèles simplistes.

2.3 L'instrumentation Čerenkov

2.3.1 Principe de la détection

En arrivant dans l'atmosphère, les rayons gamma vont créer une gerbe électromagnétique et déposer leur énergie comme dans un calorimètre. Les particules secondaires de la gerbe vont ensuite créer un flash Čerenkov, d'une durée inférieure à 10 ns dans la gamme de fonctionnement de H.E.S.S. [1]. C'est cette lumière Čerenkov qui sera détectée par les télescopes. Pour ce faire, les télescopes ont une structure particulière : ils disposent d'une surface de miroirs qui vont renvoyer la lumière Čerenkov vers une caméra constituée de photomultiplicateurs. L'électronique utilisée doit être très rapide, afin de pouvoir détecter le flash très bref. Ainsi, l'image de la gerbe va être reproduite sur la caméra à travers son émission Čerenkov. Les gerbes éléctromagnétiques sont régulières et symétriques par rapport à l'axe de propagation, leur image sur la caméra va donc avoir une forme elliptique, contrairement aux gerbes hadroniques créées par les rayons cosmiques et qui constituent le principal bruit de fond. De plus, la plupart des observatoires Čerenkov disposent de plusieurs télescopes, cette image va donc être observée en stéréoscopie, c'est à dire qu'on va la voir sous plusieurs angles. Ainsi, on pourra remonter plus facilement à la direction du gamma incident, qui se situe le long de l'axe de la gerbe, donc le long du grand axe de l'ellipse. Avec plusieurs images, la direction du gamma incident correspond donc à l'intersection des axes des ellipses.

2.3.2 Déroulement de l'analyse

Nettoyage des images et pré-coupures.

On applique un système de "double seuil" aux pixels et à leurs plus proches voisins afin d'éliminer les pixels isolés et de conserver les "amas" correspondants aux images de la gerbe et sur lesquels on calcule des moments du second ordre. On utilise ensuite des coupures d'intensité minimale et de distance entre le centre de gravité des images et le centre de la caméra afin de garder uniquement de bons candidats potentiels pour la reconstruction (images bien visibles et non tronquées).

Reconstruction.

La reconstruction consiste à calculer des paramètres intrinsèques des événements (hauteur du maximum de gerbe, paramètre d'impact [2],...) afin de remonter à la direction et à l'énergie du gamma incident. Il existe plusieurs méthodes de reconstruction [3], chacune ayant ses caractéristiques propres. La plus ancienne, dite de *Hillas*, est basée sur des moments du second ordre, les paramètres de Hillas des images sur les caméras : longueur et largeur de l'image, distance entre la direction reconstruite et la direction réelle de la source (notée θ^2), etc. Cette méthode prend en compte uniquement des paramètres simplifiés de l'image mais elle a fait ses preuves dans l'efficacité de la discrimination du bruit de fond constitué par les hadrons [2] et de part la rapidité de son algorithme. Une autre méthode développée plus récemment, appelée *Model3D*, considère une ellipsoïde de révolution à partir de laquelle sont émis les photons Čerenkov. Elle prédit ensuite les images sur les caméras en fonction de paramètres intrinsèques de la gerbe (largeur et hauteur du maximum de gerbe, ...) et compare ces prédictions aux images observées. Elle utilise toute l'information donnée dans les images et est basée sur un fit de maximum de vraisemblance, ce qui prend malheureusement plus de temps de calcul.

Création de cartes et de spectres.

En sommant toutes les directions de gamma incidents dans un champ de vue donné, on obtient des cartes du ciel. Deux types de cartes sont importantes : les cartes d'excès vont permettre d'étudier la morphologie des sources et les cartes de significativité nous assurent

1. High Energy Stereoscopic System

2. Distance entre l'impact de la gerbe au sol et le centre du réseau de télescopes.

que ces sources ne sont pas des fluctuations du fond. On définit pour cela une région On où l'on observe un signal, et une ou plusieurs régions Off dans lesquelles on supppose qu'il n'y a pas de signal. On calcule ensuite l'excès comme : $Exc = N_{On} - \alpha N_{Off}$, où N_{On} et N_{Off} sont le nombre d'événements dans les régions On et Off, et α correspond aux rapport des surfaces entre les régions. Ceci permet de nous affranchir du bruit de fond des électrons cosmiques, indiscernables des rayons gammas car ils forment eux aussi des gerbes électromagnétiques. La création de spectres sur une source donnée permet quant à elle de comparer les flux observés aux prédictions des modèles théoriques.

2.4 Amélioration de la résolution angulaire

La résolution angulaire est définie à partir de la distribution du θ^2, paramètre de Hillas correspondant à la distance entre la source réelle et sa direction reconstruite. On définit donc la résolution angulaire par le R_{68}, correspondant à 68% de cette distribution. Pourquoi améliorer la résolution ? L'expérience H.E.S.S. fonctionne depuis 2004 et les sources les plus brillantes ont d'ores et déjà été détectées. Cependant, avec une meilleure résolution angulaire, ces sources pourront être ré-analysées plus finement, au niveau de leur morphologie par exemple. De plus, cela pourrait permettre de découvrir de nouvelles sources plus faibles non encore détectées. Les différentes méthodes de reconstruction étant sensibles à différents paramètres et fluctuations, elles peuvent donner une meilleure résolution angulaire pour certains jeux de paramètres donnés. C'est donc autour de cette idée que j'ai tenté d'améliorer la résolution avec les méthodes déjà existantes.

1ère étape : simulations

On utilise des simulations de gerbes électromagnétiques à différentes efficacités optiques [3], angles zénithaux et offsets (distance entre la direction de la source et le centre de la caméra). Pour chaque simulation, on reconstruit les événements avec les deux méthodes décrites précédemment ($Hillas$ et $Model3D$), on applique ensuite un jeu de coupures donné (intensité, largeur de l'image, ...) et on calcule le R_{68} correspondant pour chaque méthode en fonction de la hauteur du maximum de gerbe $Hmax$ et de la multiplicité des télescopes. On définit ensuite la variable $Kappa$:

$$\kappa = \frac{2(R_{68}(M3D) - R_{68}(Hillas))}{R_{68}(M3D) + R_{68}(Hillas)} \qquad (2.1)$$

et on crée des tables de κ lissées en fonction de $Hmax$ pour toutes les configurations disponibles [efficacité optique, angle zénithal, offset] et pour différentes multiplicités. Ces tables de κ lissées constituent un opérateur binaire, c'est à dire qu'elles indiquent seulement quelle méthode obtient la meilleure résolution dans la configuration donnée : si $\kappa > 0$, c'est la reconstruction $Hillas$ qui a une meilleure résolution et inversement, si $\kappa < 0$, c'est $Model3D$.

2ème étape : utilisation des tables

En fonction des paramètres des événements mesurés (ou simulés), on va regarder les tables correspondantes indiquant quelle méthode de reconstruction utiliser. Avec cet algorithme de choix, pour la configuration (efficactité optique=70%, offset=1.5°) et avec des coupures optimisées pour des sources assez fortes, on obtient une amélioration de 10% de la résolution angulaire moyennée sur tous les angles zénithaux.

Ces résultats sont donc prometteurs, mais il reste cependant à appliquer cet algorithme sur des données réelles afin de vérifier l'amélioration attendue.

2.5 Etude d'un reste de supernova : G22.7-0.2

Après avoir passé en revue tous ces détails techniques, faisons un peu d'analyse de données. Il existe des catalogues recensant différents types d'objets, comme le catalogue de Green, qui compte 274 restes de supernovae (SNRs) observés dans différentes longueurs d'onde. Les SNRs sont de bons candidats accélérateurs de rayons cosmiques, comme nous l'avons vu précédemment. Or, nos observations de SNRs n'ont pas pu déterminer de facon univoque la nature des particules accélérées dans ces objets. C'est pourquoi il est intéressant d'étudier de manière approfondie les SNRs émettant en gamma.

Le reste de supernova G22.7-0.2 présente une coquille en radio, de 26 arcmins de diamètre, et est situé juste à côté d'un autre SNR : G23.3-0.3, plus connu sous le nom de W41. Comme on le voit sur la figure 2.1, W41 est étendu et très brillant en gamma, alors que l'émission gamma observée sur G22.7-0.2 est localisée sur le bord nord-est de la coquille (a). Un excès peu significatif est également observé près du bord sud (b).

Jusqu'à présent, aucune observation n'a permis de déterminer à quelle distance se trouve G22.7-0.2, mais on connait la distance de W41, qui est d'environ 4.2 kpc. De plus, les observations infrarouge montrent une probable zone d'interaction entre les deux SNRs (cavité H_{II} excité par les chocs créés lors de l'expansion des SNRs) [4]. Il semblerait donc que les deux SNRs soient assez proches l'un de l'autre.

Enfin, comme le montre la figure 2.2, les nuages moléculaires de ^{13}CO mesurés à 76 $km.s^{-1}$ sont coïncidents avec les excès (a) et (b) observés en gamma autour du reste de supernova G22.7-0.2. Or, d'après les courbes de rotation de notre galaxie [5], cette vitesse peut correspondre à deux distances possibles : 4.8 kpc ou 10.5 kpc. Dans l'hypothèse de l'interaction entre les deux SNRs, la première distance de 4.8 kpc semble donc la plus probable, et c'est celle-ci que nous utiliserons par la suite.

Comme il n'y a aucun pulsar détecté dans ce reste de supernova susceptible de fournir l'énergie nécessaire

3. L'efficacité optique dépend de la réflectivité des miroirs et de l'efficacité des PMTs, elle diminue au cours du temps et est donc définie par rapport à l'efficacité optique initiale de l'instrument.

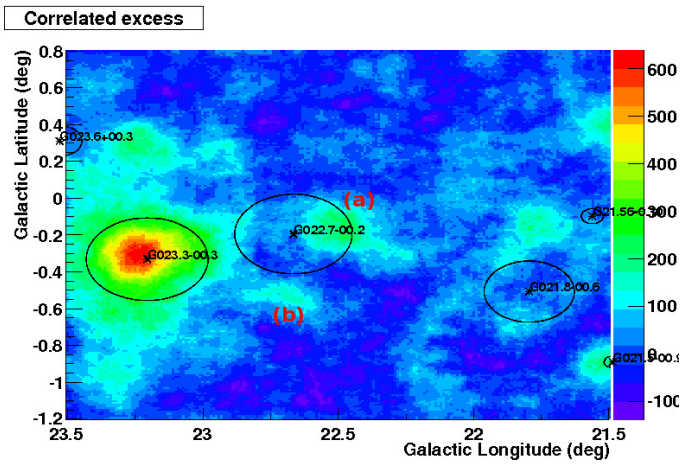


FIGURE 2.1 – Carte d'excès vu par H.E.S.S. en coordonnées glactiques. En noir : les SNRs du catalogue de Green.

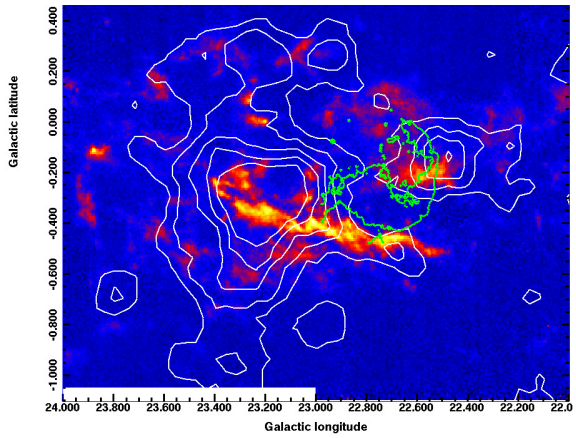


FIGURE 2.2 – Données ^{13}CO du Galactic Plane Survey (BU-FCRAO) à 76 $km.s^{-1}$. En blanc : contours de la carte d'excès de H.E.S.S., en vert : le SNR G22.7-0.2 observé en radio par les télescopes de VLA.

à l'accélération des particules chargées, une hypothèse possible pour expliquer l'émission gamma observée serait celle de l'accélération de rayons cosmiques dans l'onde de choc du SNR. En s'échappant du reste de supernova, ces derniers auraient intéragi dans les nuages moléculaires de ^{13}CO environnants et donné lieu à l'émission gamma observée par production de pions neutres.

A l'aide des données ^{13}CO et en supposant que les nuages sont à une distance de 4.8 kpc, on peut estimer leur densité n [7]. Dans l'hypothèse des rayons cosmiques accélérés dans le SNR interagissant avec ces nuages de densité n, le flux gamma F_γ attendu au dessus d'une énergie E_0 et pour un spectre en loi de puissance d'indice 2.1 est donné par [6] :

$$F_\gamma(E > E_0) \approx 9 \times 10^{-11}\ \theta\ \left(\frac{E_0}{1TeV}\right)^{-1.1}\left(\frac{E_{SN}}{10^{51}erg}\right) \times\left(\frac{d}{1kpc}\right)^{-2}\left(\frac{n}{1cm^{-3}}\right)\ cm^{-2}s^{-1} \quad (2.2)$$

où θ est la fraction de l'énergie E_{SN} de l'explosion de la supernova disponible pour l'accélération des cosmiques et d la distance mesurée du SNR. Connaissant le flux gamma observé au-dessus de $E_0 = 1\ TeV$ et en prenant $E_{SN} = 10^{51}\ erg$, on peut remonter à la fraction d'énergie θ de la supernova nécessaire pour accélérer les rayons cosmiques afin d'expliquer l'émission gamma observée

On obtient ainsi une valeur de $\theta \simeq 4\%$ de l'énergie de la supernova nécessaire à l'accélération des rayons cosmiques, ce qui est tout à fait en accord avec la fraction de 10% habituellement utilisée dans les modèles théoriques. L'hypothèse d'accélération des rayons cosmiques dans ce reste de supernova semble donc vraisembable.

2.6 Conclusion

Mes travaux sur l'amélioration de la résolution angulaire semblent prometteurs et pourraient permettre de réaliser des études morphologiques plus fines sur des sources déjà connues et peut-être de découvrir de nouvelles sources plus faibles. Concernant le reste de supernova G22.7-0.2, l'hypothèse de l'accélération de rayons cosmiques interagissant avec les nuages environnants semble vraisemblable, il reste à présent à réaliser un spectre dans toute la gamme de longueurs d'onde afin de tester si un modèle hadronique peut expliquer les flux observés.

Remerciements

Je tiens à remercier chaleureusement l'ensemble des organisateurs et coordinateurs pour leur bonne humeur et leur disponibilité ainsi que tous les participants à ces JJC 2010. Une petite pensée émue également pour les chansons de J-S, la playlist de Pedro, l'inventeur du Cointreau, les blagues belges et les histoires de québécois !

Références

[1] E. Fermi, et al., Phys. Rev. 75, 1169 (1949)

[2] A. M. Hillas, Čerenkov light images of EAS produced by primary gamma rays and by nuclei, proceedings de la 19ème conférence ICRC (1985)

[3] M. de Naurois, Analysis methods for atmospheric Čerenkov Telescopes, Astro-ph (2006)

[4] W. T. Reach et al., A Spitzer Space Telescope infrared survey of supernovae remnants in the inner galaxy, Astronomical Journal (2006)

[5] D. P. Clemens et al., Massachusetts-Stony Brook Galactic Plane CO Survey : The galactic disk rotation curve, ApJ (1985)

[6] L. Drury, F. Aharonian, H. Voelk, The gamma-ray visibility of supernova remnants, A&A (1993)

[7] R. Simon et al., The structure of four molecular cloud complexes in the BU-FCRAO Milky Way Galactic Ring Survey, ApJ (2001)

Extracting Aerosol properties by the Central Laser Facility at the Pierre Auger Observatory



Karim Louedec
Laboratoire de l'Accélérateur Linéaire, Univ Paris-Sud, CNRS/IN2P3, Orsay, France.

Résumé

The atmospheric monitoring is essential in Auger to reduce errors on the estimation of the shower energy. The goal here is to develop a new method to extract all along the night parameters characterizing the aerosol component. The extracting procedure is presented and tested on simulated events.

3.1 Introduction

The Pierre Auger Observatory detects the highest energy cosmic rays with over 1600 water-Cherenkov detectors arranged as an triangular array. It is surrounded by the fluorescence detector (FD) which consists of 24 fluorescence telescopes grouped in units of 6 at four locations. The telescopes measure fluorescence emission from the atmosphere due to the crossing of electrons and positrons produced in the air shower. Each telescope consists of a mirror with a camera at its focal plane, composed of 440 photomultipliers. Each pixel is a hexagon with a typical diameter equal to 1.5°. In front of this setup, a diaphragm of diameter equal to 2.2 meters coupled to a UV filter is placed. Thanks to an absolute pixel calibration, the signal recorded by the camera can be converted in UV photon number. Since the fluorescence light is proportional to the energy deposited by the shower, the primary cosmic ray energy can be estimated if the fluorescence yield is known.

The originality in the Auger experiment is that the atmosphere is used as a giant calorimeter. Of course, to get a shower reconstruction as accurate as possible, it is necessary to have a large atmospheric monitoring program [1]. Two main physical quantities have to be estimated to correct the effect of the atmosphere to the number of photons detected by the telescopes : the attenuation length being linked to the concentration, and the phase function [1] estimating the scattering properties. Usually, the atmospheric light scattering problem is split into two regimes according to the ratio between the incident light wavelength and the target size : the molecular scattering (or *Rayleigh scattering*) mainly due to nitrogen and oxygen molecules, and the aerosol scattering (or *Mie scattering*) due to particles much larger than the Angstrom and coming from different sources (mainly from soil).

1. The phase function can be seen as the differential cross section normalized to the total cross section for photon scattering, it means $(1/\sigma) \times (\mathrm{d}\sigma/\mathrm{d}\Omega)$.

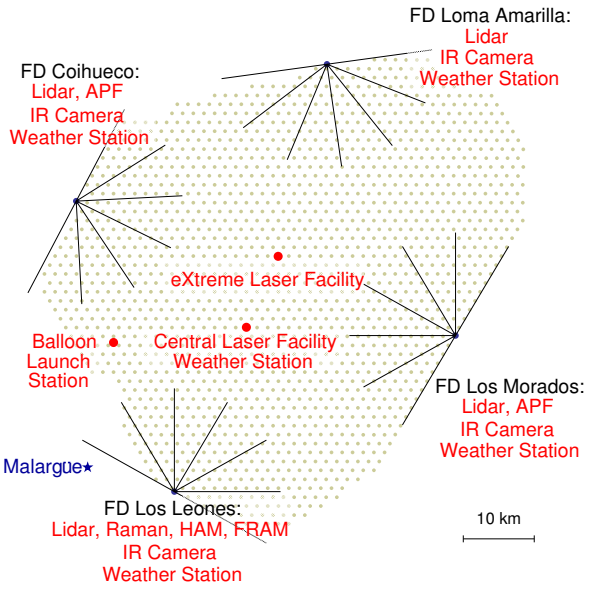


FIGURE 3.1 – **Map of the Pierre Auger Observatory located close to Malargüe in Argentina.** Several atmospheric setups are used by the collaboration, sometimes present in several times, one at each FD site.

Figure 3.1 lists the different experimental setups that have been installed at Malargüe to monitor the atmosphere. Lot of them refer to the aerosol measurement : when the molecular part can be considered more or less unchanged all along the night, it is not the case for the aerosols. They are strongly dependent on time, climate and location. 4 Lidar systems and a procedure based on the vertical laser shots are operational to estimate the aerosol concentration on the Malargüe site. Also, according to the Mie theory, the Aerosol Phase Function (APF) depends on the size distribution and shape of the particles. Thus, it is needed to have an APF monitoring all along the night to estimate properly the aerosol scattering properties. Up to now, the APF estimate in Auger consists into two UV light sources operating at Coihueco and Los Morados FD sites [2].

The purpose of this note is to develop a new method to monitor all along the night the two main aerosol parameters, the Aerosol Phase Function (linked to the aerosols size) P_{Mie} and the corresponding attenuation length Λ_{Mie}. The method consists in using the Central Laser Facility (CLF) and especially its ability to fire laser shots in any direction.

3.2 The Central Laser Facility

The Central Laser Facility (CLF) is barely located at the middle of the Auger surface detector. The facility is powered by a battery charged itself by thirteen solar panels, generating a maximum power of 885 Watts [3]. The wavelength is 355 nm, in the middle of the nitrogen fluorescence spectrum that is produced by air showers. The beam is pulsed with a width of 7 ns and a maximum energy per pulse around 6.5 mJ. To estimate the relative energy of each laser pulse, a portion of the beam is diverted into a photo-diode detector. The beam light is headed towards the sky. Nevertheless, a mirror can send the light to a steering head mounted on the roof of the container. It consists of two rotating mirrors allowing to point the beam towards any direction above the horizon.

The zenith angle $\theta_{\rm FD}$ is defined as equal to 0° when the laser shot is horizontal, and equal to 90° when it is vertical. The azimuth angle $\phi_{\rm FD}$ uses as reference the CLF azimuth angle allowing to "shot-the-head" of the FD eye. While selecting the laser shots to fire, there is a dilemma between the low scattering angle reached for the APF reconstruction and the time spread for the collected light profile. Indeed, a too short light profile in time could not trigger the FD eyes during the data acquisition. In this note, only the laser shot ($\theta_{\rm FD} = 3^{\rm o}$, $\phi_{\rm FD} = +6^{\rm o}$) will be studied : it allows to extract the APF over a large range of scattering angles, from scattering angles around 10° to 100°. From these shots, it could be possible to draw the minimum of the APF. Another reason for this choice is that they are already fired every night at Malargüe for every FD buildings. Figure 3.2 draws its FD camera display and the light profile expected for typical atmospheric conditions. The discontinuities in the light profiles come from the overlap in the fields of view of pixels located at the transition between two telescopes : the real signal is about one half of the jump signal.

3.3 Extracting of the Aerosol Phase Function

The Central Laser Facility accompanied by the fluorescence detectors can be used to measure the APF all along the night during FD data taking. The APF can then be reconstructed from the intensity of the light observed by the FD cameras as a function of the scattering angle ζ. Following the position of the recorded signal in the cameras, different scattering angles can be reachable. The signal from the CLF shot observed by the ith pixel of the fluorescence detector can be expressed as Equation 3.1, where I_0 is the original light beam intensity, ζ the scattering angle corresponding to the ith pixel, Δz_i the laser track length observed by the pixel and $\Delta\Omega_i$ the solid angle. The physical quantities inside the brackets $\langle X \rangle_{\Delta z_i}$ means that their value changes during the travel. Thus, for each pixel, we have to use their mean value averaged over the whole track length corresponding to the ith pixel.

$\Lambda_{\rm Ray}$ and $\Lambda_{\rm Mie}$ are the molecular attenuation length and the aerosol attenuation length, respectively. Their value change exponentially as a function of the altitude. The vertical scale is around 8 km for the molecular component (from the US Standard atmospheric model) and is fixed by $h_{\rm Mie}$ for the aerosol component. $T_{\rm Ray}$ and $T_{\rm Mie}$ are the molecular attenuation factor and the aerosol attenuation factor, respectively. Since the travelled length are too different from one pixel to another one, the attenuation factors can not be removed from Equation (3.1).

$P_{\rm Ray}(\zeta)$ and $P_{\rm Mie}(\zeta)$ are the phase functions for the molecular scattering and the aerosol scattering. They are defined in a sense that their integral over all solid angles has to be equal to one. From the Rayleigh scattering theory, the analytical phase function well known is given by

$$P_{\rm Ray}(\zeta) = \frac{3}{16\pi(1+2\gamma)}\left[(1+3\gamma) + (1-\gamma)\cos^2\zeta\right], \tag{3.2}$$

where γ includes the effect of molecular anisotropy in Rayleigh scattering. In Auger, its value is fixed at 0.03 for our wavelength.

From the Mie scattering theory, it does not exist an analytical function to describe the scattering. Thus, it is needed to use parameterizations which are only approximations of the exact solutions. In our case, the Henyey-Greenstein parameterization will be used [4]. It is defined as follows

$$P_{\rm Mie}(\zeta) = \frac{1-g^2}{4\pi}\frac{1}{(1+g^2-2g\cos\zeta)^{3/2}}, \tag{3.3}$$

where $g = \langle\cos\theta\rangle$ is an asymmetry parameter. The possible values for g go from $g = 1$ in the case of a total forward scattering to $g = -1$ for a total backward scattering.

3.3.1 Geometry reconstruction of the laser shots

The goal of this geometry reconstruction is to affect to each pixel its scattering angle and its correction factors which will be needed to reconstruct the APF from the signal collected by the FD eyes. At each step $L_{\rm step}$, the program registers which pixels are able to collect signal from the laser location while including a spread function of 0.25° to describe the aberration effects due to mirror optics. For each triggered pixel, these different operations are done : its track length is incremented by the $L_{\rm step}$ value, and the scattering angle, the solid angle, the total travelled length, the altitude, the Rayleigh attenuation factor, the Rayleigh attenuation length, etc... are added to their own vectors defined for each of these parameters. At the end of the travel, its track length Δz_i is directly obtained and the other geometrical quantities are only the mean of the values stored in the corresponding vector.

Let's see how the reconstruction geometry algorithm works thanks to the laser shot ($\theta_{\rm FD} = 3^{\rm o}$, $\phi_{\rm FD} = 6^{\rm o}$) at

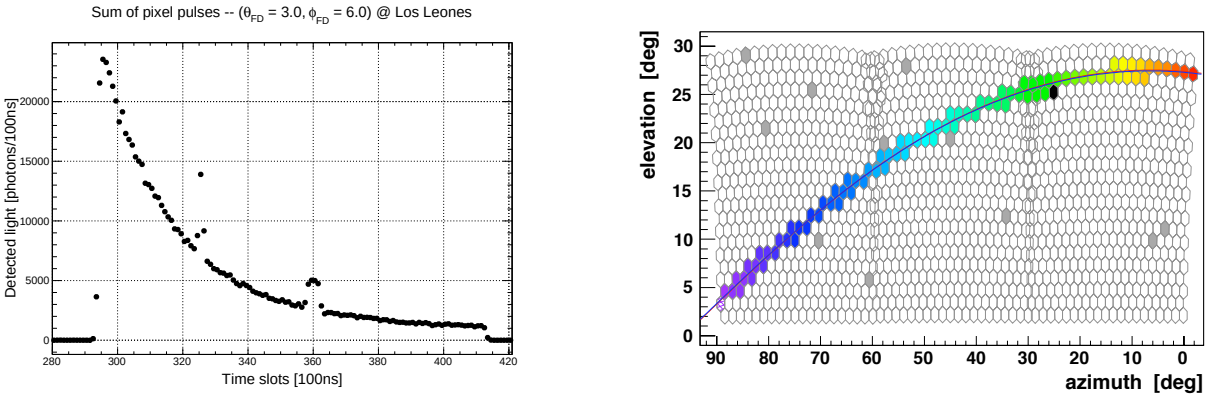


FIGURE 3.2 – **Laser shot ($\theta_{\rm FD} = 3^{\rm o}$, $\phi_{\rm FD} = +6^{\rm o}$) @ Los Leones.** *Left panel :* Light time profiles, averaged over 15 shots, expected from simulations. *Right panel :* Event display expected on the FD camera. The colour code gives the timing of the shot, blue colour being the beginning and the red colour representing the end of the time profile.

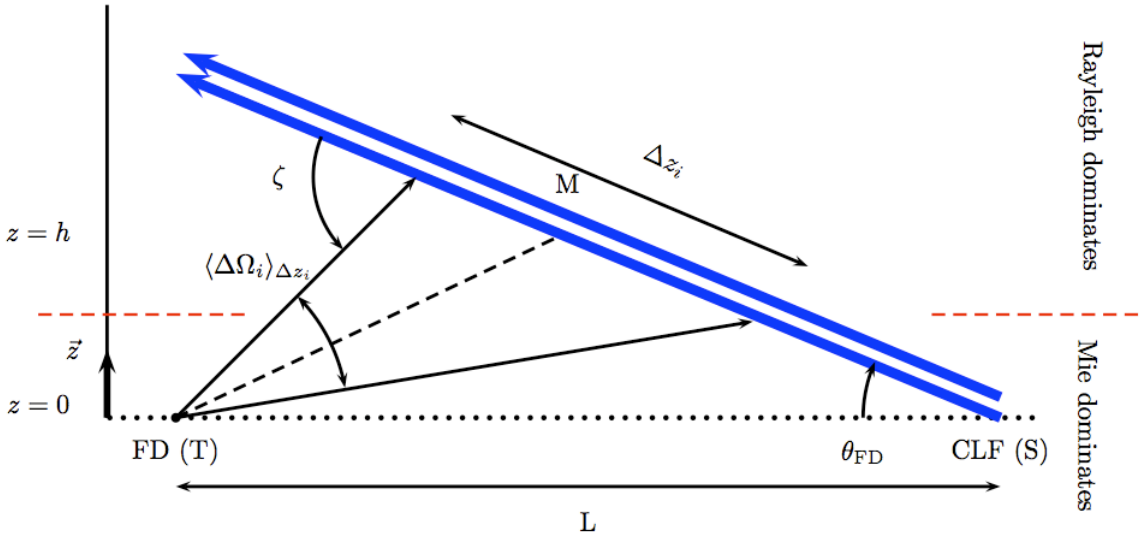


FIGURE 3.3 – **Sketch of the experimental setup with the CLF seen by one FD eye.** L represents the length between the source point S, or CLF, and the detector point T, or FD telescope. M is the point along the laser axis at the step j. The dashed red line displays barely the two regions where the Mie scattering dominates in the low altitude layer and where the Rayleigh scattering dominates at high altitude.

$$S_i = I_0 \times \langle T_{\rm Ray} \rangle_{\Delta z_i} \times \langle T_{\rm Mie} \rangle_{\Delta z_i} \times \left[\frac{1}{\langle \Lambda_{\rm Ray} \rangle_{\Delta z_i}} P_{\rm Ray}(\zeta) + \frac{1}{\langle \Lambda_{\rm Mie} \rangle_{\Delta z_i}} P_{\rm Mie}(\zeta) \right] \times \Delta z_i \times \langle \Delta\Omega_i \rangle_{\Delta z_i}, \qquad (3.1)$$

Los Leones. The three main geometrical quantities are given in Figure 3.4 : the solid angle, the track length and the Rayleigh attenuation factor. They are plotted with respect to the scattering angle (in other words, each reconstructed pixel corresponds to one unique scattering angle). Whereas the Rayleigh attenuation does not change much with the scattering angle, the track length is very sensitive at the lowest scattering angles. The solid angle behaviour shows that the lowest distance FD-laser is reached for a scattering angle around 90°. Since the accuracy on the azimuth angle is around 0.2° for the CLF, the geometrical quantities for $\Delta\phi_{\rm FD} = \pm 0.2^{\rm o}$ are also plotted to show our sensitivity to this systematic.

3.3.2 Description of the APF reconstruction procedure

Only the factor I_0, specific to the detector, can not be estimated by the program. Thus, it is estimated thanks to a Rayleigh night, it means a night where the atmosphere scattering can be reproduced only with the molecular contribution. In a such night, all the parameters, excepted I_0, are known in Equation 3.1 and can be reconstructed. By this way, it becomes doable to estimate the I_0 factor.

Now, it becomes possible to estimate the parameters linked to the aerosols in the atmosphere. The APF reconstruction procedure follows these steps. From the

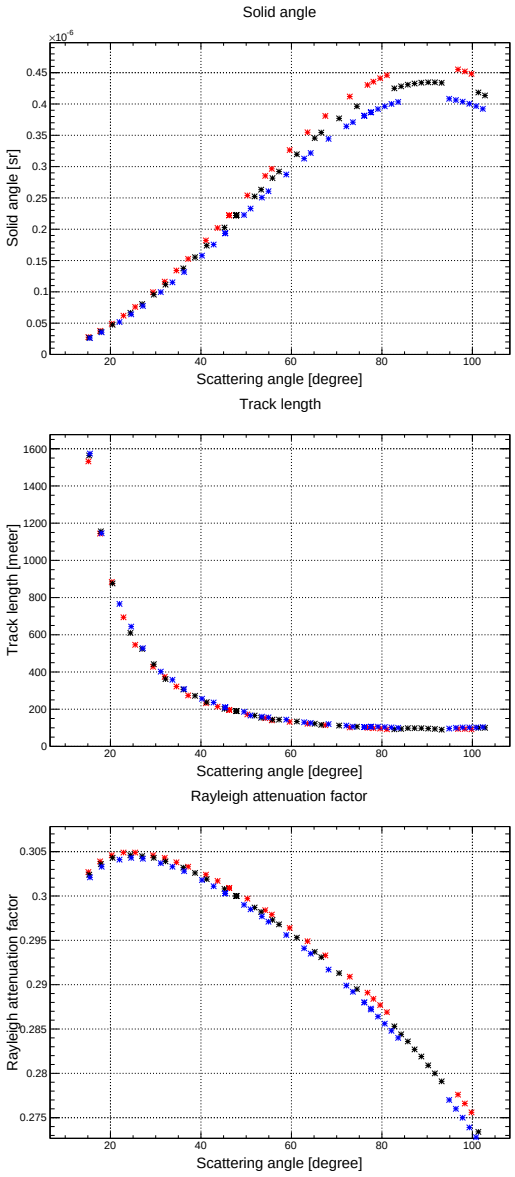


FIGURE 3.4 – **Parameters estimation for the laser shot ($\theta_{\mathrm{FD}} = 3^{\mathrm{o}}$, $\phi_{\mathrm{FD}} = 6^{\mathrm{o}}$) @ Los Leones.** The track length Δz_i, the solid angle $\langle \Delta\Omega_i \rangle_{\Delta z_i}$ and the Rayleigh attenuation factor $\langle T_{\mathrm{Ray}} \rangle_{\Delta z_i}$ are plotted as a function of the scattering angle (or for each triggered pixel). The black dots are for the case where $\Delta\phi_{\mathrm{FD}} = 0^{\mathrm{o}}$, the red dots for $\Delta\phi_{\mathrm{FD}} = +0.2^{\mathrm{o}}$ and the blue ones for $\Delta\phi_{\mathrm{FD}} = -0.2^{\mathrm{o}}$.

input file, the light collected by the triggered pixels is extracted. We assign to each pixel a signal value S_i. For each ith pixel, we divide its signal by the correction factors and by the source factor :

$$S_i' = S_i / \left(I_0 \times \langle T_{\mathrm{Ray}} \rangle_{\Delta z_i} \times \Delta z_i \times \langle \Delta\Omega_i \rangle_{\Delta z_i} \right).$$

We get a new signal value S_i' depending only on the aerosol parameters, that are $\{g,\ \Lambda_{\mathrm{Mie}},\ h_{\mathrm{Mie}}\}$. Finally, the binned laser shot signal observed in the FD eyes is subjected to a 3-parameter fit. The method employed is to simulate expected profiles for each $\{g,\ \Lambda_{\mathrm{Mie}},\ h_{\mathrm{Mie}}\}$ configuration. Then, a χ^2 test is run and estimates

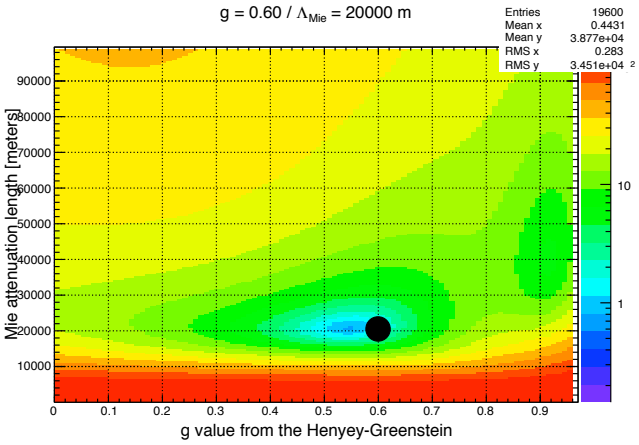


FIGURE 3.5 – **Minimization of the χ^2 for the laser shot ($\theta_{\mathrm{FD}} = 3^{\mathrm{o}}$, $\phi_{\mathrm{FD}} = 6^{\mathrm{o}}$) @ Los Leones.** True values are given by the black point and the estimated values are in the blue area.

which are the best parameters to overlap the profile.

Figure 3.5 displays a χ^2 minimization procedure on a simulation. The true aerosol parameters are given by the black circle, here $g = 0.6$ and $\Lambda_{\mathrm{Mie}} = 20$ km. Our program gives a minimized χ^2 for parameters more or less with the same values (blue area on the plot). A complete simulation set has already been produced for different $\{g,\ \Lambda_{\mathrm{Mie}}\}$ values and the APF reconstruction procedure has been applied on it. The most important point is that this method is sensitive for Λ_{Mie} values lower than around 40 km. For values higher, the light profile does not change enough to distinguish any aerosol parameters modification.

Conclusion

All along this note, it has been shown how the understanding of the properties of the atmosphere is a key point. Also, a new method to estimate the aerosol population has been developed and tested on simulations. The next step before the end of my thesis is to apply it on CLF data, the final goal being to monitor aerosols all along the night.

Acknowledgments

I would like to thank the awesome organizers for this week at Angers (you know, the city close to Bretagne). Even if the food was not so good (contrary to the drinks), it was a pleasure to share our feelings between PhD students. And when I see the evenings spent there, I can tell you that the IN2P3 has a great future. See you soon for the next JJC or/and JRJC !

Références

[1] The Pierre Auger Coll 2010 *Astroparticle Physics* **33** 108-129

[2] BenZvi S *et.al.* 2007 *Astroparticle Physics* **28** 312-320

[3] Fick B *et.al.* 2006 *JINST* **1** 11003

[4] Henyey LG and Greenstein JL 1941 *Astrophys. J.* **93** 70-83



Search for large-scale anisotropies in the distribution of cosmic rays with the Pierre Auger Observatory

Moritz Münchmeyer
Laboratoire de Physique Nucléaire et de Hautes Energies, Paris

Résumé

The Pierre Auger Observatory is the worlds largest detector for Ultra High Energy Cosmic Rays. It offers a data set suitable for the search for large-scale anisotropies in the distribution of Cosmic Rays at the percent level. We review analysis techniques, both for 1-dimensional and 2-dimensional large-scale anisotropy search, and discuss the dominant systematics. Recent results for the first harmonic analysis are presented. Finally the geomagnetic effect is studied as a prerequisite for the 2-dimensional analysis.

4.1 Introduction

Cosmic Rays (CR) can be defined as particles, such as protons or nuclei, travelling through interstellar space. Knowing the properties of these particles can help to evaluate models of their sources and their distribution in the universe, as well as the magnetic fields that influence their propagation through space. When these particles interact with the atmosphere, a large air shower of secondary particles is created. Cosmic Rays thus also give indirect information on particle physics at ultra high energies.

Together with the energy spectrum and the composition (i.e. the particle types), the distribution of the arrival directions is a major observable for Cosmic Ray physics. Generally we can divide the search for anisotropies in two separate tasks : Search for point sources and search for large-scale anisotropies. The former is be done by looking at the arrival directions of the events with the highest energies. At the highest energies (above 6×10^{19} EeV), the Auger Observatory reported a correlation of 69 events with the nearby extra-galactic matter distribution within 75 Mpc around the Milky Way [1].

Large-scale anisotropy analysis on the other hand compares the flux from different regions of the sky, using thousands of showers. Some models predict a dipolar anisotropy determined by the local magnetic field and the density gradient of cosmic rays in the galaxy [2]. A change in the anisotropy pattern at a certain energy could be due to a transition from galactic to extragalactic CRs. A general absence of anisotropy at lower energies would point to strong galactic magnetic fields that isotropize the arrival directions.

In this article, we give a brief discussion of the experiment, and then describe in section 4.3 techniques and systematic effects for the search for large-scale anisotropies in one space dimension. We review the experimental results for this methods, as recently published by the Auger collaboration [3]. In section 4.4, we describe the multipolar method to search for anisotropies in two space dimensions, and examine the effect of the geomagnetic field on such an analysis.

4.2 The Pierre Auger Observatory

The Pierre Auger Observatory [4] is a large detector array for cosmic rays located in the Pampa Amarilla in western Argentina. With its huge size of about 3000 km^2, it is able to study cosmic rays of high energies above 1 EeV efficiently. Its main objective is to measure the flux, arrival direction distribution and mass composition of cosmic rays from 10^{18} eV up to the highest energies. The Pierre Auger Observatory uses a hybrid detection technology consisting of 1660 water tanks arranged in a triangular grid (the surface detector array SD) and 4 optical detector stations (the fluorescence detector FD). The FD telescopes measure the fluorescence light emitted along the path of the air showers and thus traces their longitudinal development. The SD, which will be used in this analysis, detects the secondary particles of the extended air showers arriving at ground level and therefore samples the lateral density distribution of the air shower on the ground.

In the SD reconstruction process, the direction of the CR is obtained by fitting the shower front to the arrival times of the signals in the tanks. It reaches an angular resolution of about $1 - 2\%$, depending on primary energy and zenith angle. The energy determination is obtained by fitting a shower profile, deriving the signal strength S1000 at 1000m from the shower core, normalizing it to a fixed zenith angle (38°) and then using a calibration curve based on the fluorescence measurements. In the energy range of 1 EeV, the SD has now acquired sufficient statistics to be sensible to a dipolar large-scale anisotropy with an amplitude of the order of 1%.

4.3 1-dimensional large-scale anisotropy search

The aim of the 1-dimensional method is to determine the first harmonic amplitude r and its phase ϕ in the right ascension distribution of cosmic rays. Com-

pared to a 2-dimensional method, where one considers the arrival direction distribution in right ascension and declination, this has the experimental advantage of not depending on precise knowledge of the exposure dependency on declination.

4.3.1 Rayleigh and East-West method

There are two basic methods that are currently used by the Auger collaboration for 1-dimensional large-scale anisotropy search, the Rayleigh method [5] and the East-West method [6]. In the classical Rayleigh analysis, we do a Fourier Transformation to extract the first harmonic amplitude in the right ascension distribution α_i of the events. The normalized Fourier coefficients are given by

$$a = \frac{2}{W}\sum_i w_i \cos\alpha_i, \qquad b = \frac{2}{W}\sum_i w_i \sin\alpha_i \quad (4.1)$$

where w_i are weights correcting for the non-uniform detector coverage, to be specified below and W is the normalization constant.

The amplitude r and phase ϕ are given by

$$r = \sqrt{a^2+b^2}, \qquad \phi = \arctan\frac{b}{a} \quad (4.2)$$

The deviations from an uniform event rate in right ascension being small, the probability $P(>r)$ that an amplitude equal or larger than r arises from a uniform distribution can be approximated by the Rayleigh distribution

$$P(>r) = \exp(-Wr^2/4).$$

At low energies $E < 1\%$, the Auger data set offers large statistics, but the detection efficiency for these showers depends strongly on zenith angle and composition. At these energies, it is therefore preferable to use another analysis method, that does not depend on knowledge of the detection efficiency. This method makes use of the difference in the counting rate between the Eastward $I_E(\alpha)$ and Westward $I_W(\alpha)$ directions, both of which are equally influenced by detector instabilities and atmospheric effects. The substraction of the Western sector from the Eastern sector can be accomplished by a slight modification of the Fourier coefficients for the standard Rayleigh analysis.

$$a_{EW} = \frac{2}{N}\sum_i \cos(\alpha_i^0+\zeta_i), \quad b_{EW} = \frac{2}{N}\sum_i \sin(\alpha_i^0+\zeta_i) \quad (4.3)$$

where ζ_i is 0 for events coming from the East and π for events coming from the West. This effectively subtracts the events from the West direction. Amplitude r and phase ϕ_{EW} can be calculated as in equation 4.2, where $\phi = \phi_{EW} + \pi/2$. The East-West method needs approximately four times more events to attain the same sensitivity as the Rayleigh method.

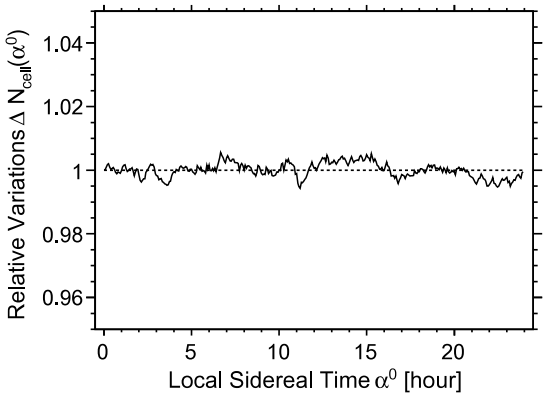


FIGURE 4.1 – Relative variation of the integrated number of detector cells as a function of local sidereal time. [3]

4.3.2 Correction of time dependent exposure and atmosphere

The instantaneous exposure of the Auger Observatory is given by

$$\omega(t,\theta,\phi,E) = n_{cell}(t) \times a_{cell}\cos\theta \times \epsilon(E,\theta,\phi) \quad (4.4)$$

where n_{cell} is the number of active detector cells, a_{cell} is the surface area of a detector cell and ϵ is the directional detection efficiency function. The number of active detector cells is a time dependent quantity, which modulates the expected event rate.

For the first harmonic analysis described above, we calculate the integrated detector cell exposure depending on local sidereal time t_{sid} (equivalent to right ascension α_0), by

$$N_{cell}(t_{\rm sid}) = \sum_j n_{cell}(t_{\rm sid} + jT_{sid}) \quad (4.5)$$

where $T_{sid} = 23h, 56m, 4s$ is the length of a sidereal day, the time of a complete rotation of the earth. To correct for this non constant exposure, we weight each event in the Fourier expansion 4.1 by $w_i = \frac{1}{\Delta N_{cell}(\alpha_i^0)}$, where ΔN_{cell} is the relative exposure modulation depicted in figure 4.1 for the approximately 5 years of data taking.

Applying necessary energy cuts in the data set adds another time dependent systematic that indirectly influences the measured event rate. Changes of pressure P and density ρ of the atmosphere influences the shower development and thus the measured signal strength in the detector tanks. As shown in [7], the reconstructed shower energy E_{rec} can be corrected a posteriori by

$$E = E_{rec} \times [1 - \alpha_P(P-P_0) - \alpha_\rho(\rho_d - \rho_0) - \beta_\rho(\rho - \rho_d)]^B \quad (4.6)$$

where α_P, α_ρ, β_ρ and B are empirically determined constants, and the atmospheric parameters are constantly measured at the Auger site. The event rate modulation due to the atmospheric effect on the energy

dependence turns out to be only of $\simeq 0.2\%$ for energies above 3 EeV. At lower energies, where the array is not fully efficient, also the detection efficiency ϵ is also influenced by the atmospheric properties. However down-to an energy of 1 EeV, the current statistics of the Rayleigh analysis are not sensible to this additional influence. At lower energies we use only the East-West method, which avoids these problems completely, though at the cost of reduced sensitivity.

4.3.3 Results

The procedure described above was applied to the SD data by the Auger collaboration in [3]. The analysis was performed using energy intervals chosen to be $\Delta \log_{10}(E) = 0.3$ below 8EeV. All events above 8EeV are gathered in a single energy interval. Figure 4.2 shows the amplitude r as a function of energy together with the 99% C.L. upper bound on the amplitude that could result from fluctuations in an isotropic distribution. The amplitudes over the whole energy range are consistent with isotropy.

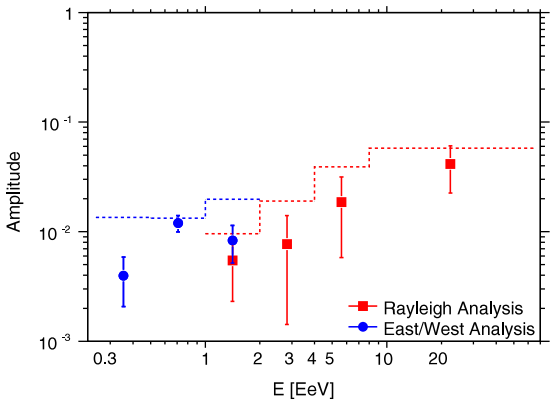


FIGURE 4.2 – Amplitude r of the first harmonic as a function of energy. Dashed line : 99% C.L. upper bound for isotropic fluctuations. [3]

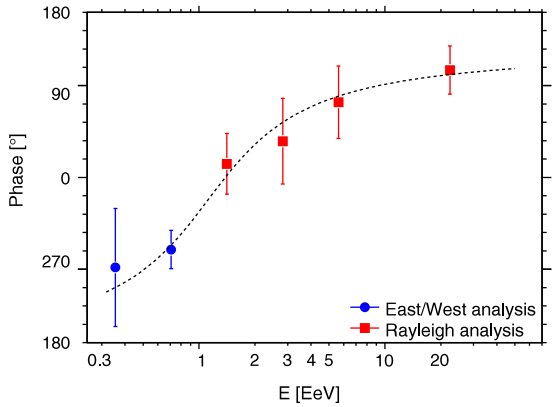


FIGURE 4.3 – Phase ϕ of the first harmonic as a function of energy. The dashed line illustrates a smooth transition. [3]

Figure 4.3 shows the phases for the same energy intervals. While the amplitudes gave no evidence for an anisotropy, the phases show an interesting correlation, that is unlikely to arrive from an isotropic background distribution. The data suggests a smooth transition between a common phase about $\alpha \simeq 270°$, in the first two bins, and another phase $\alpha \simeq 100°$ for higher energies. Note that the low energy phase points towards the galactic center $\alpha_{GC} \simeq 268.4°$, nicely corresponding to other experimental and theoretical evidence suggesting that there might be a transition from galactic to extragalactic origin at an energy of a few EeV. The above being an aposteriori analysis, it is not possible to give a confidence level on the observed smooth transition. It is however worth noting, that the phase analysis can be shown to be more sensitive to anisotropy than the detection of amplitudes. It will be interesting to compare the observed transition to future independent data.

4.4 2-dimensional large-scale anisotropy search

2-dimensional large-scale anisotropy search makes use of the full directional information (declination and right ascension) of the detected cosmic rays. We describe a method based on spherical harmonics, that generalizes the harmonic analysis in one dimension. By using a multipolar expansion, we search for dipolar, quadrupolar and higher order components of the background distribution.

The Auger Collaboration has not yet published results for this analysis, so we only present the method without applying it to data. For using the declination distribution, it is essential to understand declination dependent systematics. Dominant among these is the geomagnetic effect, which we study briefly in section 4.4.2.

4.4.1 General multipolar method

The multipolar expansion of a function $\lambda(\theta, \phi)$ is defined as

$$\lambda(\theta, \phi) = \sum_{l,m} a_{lm} Y_l^m(\theta, \phi) \tag{4.7}$$

where Y_l^m are spherical harmonics with $l = 1$ corresponding to a dipole and $l = 2$ corresponding to a quadrupole.

The coefficients a_{lm} for a set of N events probing the distribution $\lambda(\theta, \phi)$ with a uniform coverage can be estimated by

$$a_{lm} = \frac{1}{N} \sum_{i}^{N} Y_l^m(\theta_i, \phi_i) \tag{4.8}$$

However this estimator cannot be used for realistic cosmic ray observations, that have a non-uniform and partial sky coverage $\omega(\theta, \phi)$. In such an experiment, the observed distribution is the product of background distribution and coverage $\lambda(\theta, \phi)\omega(\theta, \phi)$. In [8], a modifica-

tion of the standard multipolar method was proposed, that can be applied to this situation. One possible approach is to build a new set of orthogonal functions Z_l^m by applying the Gram-Schmitt orthogonalization procedure to the product $\omega(\theta,\phi)Y_l^m(\theta,\phi)$.

$$Z_l^m(\theta,\phi) = \sum_{l'=m}^{l} C_{l'l}^m \omega(\theta) Y_l^m(\theta,\phi) \tag{4.9}$$

assuming the coverage to be uniform in right ascension. We can then expand the observed $\omega\lambda$ by

$$\omega\lambda = \sum_{l,m} \alpha_{lm} Z_l^m \tag{4.10}$$

and estimate the coefficients with

$$\alpha_{lm} = \frac{1}{N}\sum_{i}^{N} Z_l^m(\theta_i,\phi_i) \tag{4.11}$$

The original multipolar coefficients a_{lm} can be recovered from the α_{lm} by making the supposition that the true background distribution is limited to $l < L$ (corresponding to a minimal angular scale $\approx \pi/L$). In that case it is possible to estimate the a_{lm} by

$$a_{lm} = \sum_{l'=l}^{L} C_{l'l}^m \alpha_{l'm} \tag{4.12}$$

4.4.2 The geomagnetic effect

Air showers include charged particles and are thus influenced by the magnetic field of the earth. Generally, a shower will be spread in the direction of the Lorentz force, given by the shower axis and the magnetic field vector. This spread changes the measured shower signal S1000 on the ground and therefore the reconstructed energy. As an illustration of the effect, consider the μ_- muon density map in figure 4.4. It was obtained by Monte Carlo shower simulation, injecting a primary proton of 5 EeV with a zenith angle of 55°. The presence of the geomagnetic effect clearly brakes the otherwise circular symmetry. The effect is much stronger for muons than for electrons, due to their longer track length in the shower.

A simple model can provide some insights on the above effect. For a single muon in the shower, the transverse magnetic deviation can be approximated by

$$\delta_\pm = \frac{\pm qcB_T}{2}\frac{z^2}{E} \tag{4.13}$$

where q is the charge, z is the distance traveled along the shower axis and E is the energy of the muon. B_T is the component of the magnetic field transverse to the shower axis. Assuming an undeviated muon density distribution $\rho_+ = \rho_- = \rho/2$, the deviated muon

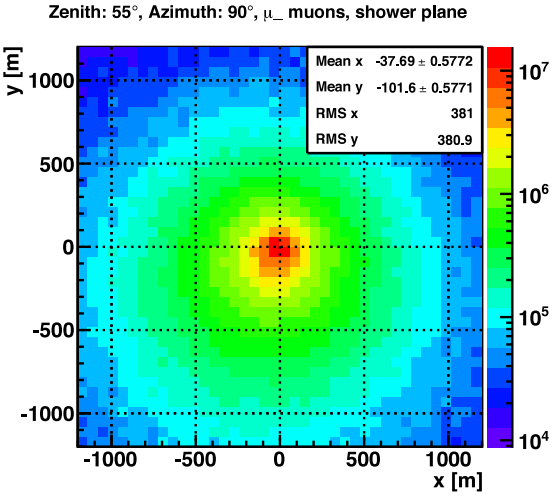


FIGURE 4.4 – μ_- muon density map in the shower plane, obtained from simulation with a realistic geomagnetic field. Primary particle : proton, 5 EeV.

distribution is

$$\rho_{\text{deviated}} = \frac{1}{2}(\rho_+(x+\delta_+) + \rho_-(x+\delta_-)) \tag{4.14}$$

$$\simeq \rho(x,y) + \frac{\delta^2}{2}\frac{\partial^2\rho}{\partial x^2}(x,y), \tag{4.15}$$

suggesting a quadratic dependence of the shift on the transverse field strength B_t.

To precisely evaluate the angular dependency of the geomagnetic effect on the shower energy, including the dependency of the shower development on the zenith angle, extensive Monte Carlo studies have been performed. The aim of these studies is to find a correction formula to the reconstructed energies, analogous to the one used for the atmospheric corrections. Such a formula will be given in [9] and is a necessary prerequisite for declination dependent anisotropy studies with a sensitivity at the percent level.

Références

[1] The Auger Collaboration, Astropart. Phys 34 (2010) 314

[2] V. Ptuskin et al., Astron. Astrophys. 268 (1993) 726

[3] The Auger Collaboration, Astropart. Phys 34 (2011) 627

[4] The Auger Collaboration, Nucl. Inst. Meth. A 523 (2004) 50

[5] P. Sommers, Astropart. Phys. 14 (2001) 271

[6] R. Bonino et al., in preparation

[7] The Auger Collaboration, Astropart. Phys 32 (2009) 89

[8] P. Billoir, O. Deligny, JCAP 0802 :009 (2008)

[9] The Auger Collaboration, in preparation

Searching for gravitational waves associated with gamma-ray bursts



Michal Was
Laboratoire de l'Accélérateur Linéaire, Orsay

Résumé

We present the general principle of gravitational wave observations, in particular in association with gamma-ray bursts. Some details on data analysis techniques used and most recent results are given.

5.1 Gravitational waves

Gravitational waves are one of the early predictions of Einstein's theory of General Relativity. However they have eluded attempts of direct observation in the past 90 years and only indirect observation are available. Radio observation of pulsars in close binary systems [1] have shown that these binary systems loose energy through gravitational radiation according to General Relativity prediction within the $\sim 1‰$ accuracy.

The theory of General Relativity describes the gravitational force through the curvature of the space-time metric, gravitational waves are a propagating perturbation of this space-time metric. These waves can be straightforwardly obtained as a solution of linearized Einstein's equation. Their fundamental properties are that they propagate at speed of light c and have two polarizations, usually called *plus* and *cross* polarization. Their main effect on an observer is the squeezing and stretching of the local space-time in two orthogonal direction in the plane orthogonal to the direction of propagation.

In first approximation the power gravitationally radiated by a body depends only on the evolution of its quadrupolar mass moment Q_{mn}

$$P_{\mathrm{GW}} = \frac{G}{5c^5} \left\langle \dddot{Q}_{mn} \dddot{Q}^{mn} \right\rangle . \tag{5.1}$$

For a body with typical size R, moving with speed v with an asymmetry $\epsilon = (Q_{xx} - Q_{yy})/Q_{zz}$ this power can be written as

$$P_{\mathrm{GW}} \propto \frac{c^5}{G} \epsilon^2 \left(\frac{R_S}{R}\right)^2 \left(\frac{v}{c}\right)^6 < 2 \times 10^5 \, \mathrm{M}_\odot \mathrm{c}^2 \mathrm{s}^{-1}, \tag{5.2}$$

where $R_S = \frac{2GM}{c^2}$ is the equivalent Schwartzschild radius of the body of mass M. Hence good sources of gravitational waves are compact $R \sim R_S$, asymmetric $\epsilon \sim 1$ and relativist $v \sim c$. In practice some astrophysical objects, such as a pair of coalescing black holes, are close to these conditions and should create fluxes much larger than any possibly produced on Earth, despite the great distances *a priori* involved ($\gtrsim 100\,\mathrm{Mpc}$).

5.2 Gravitational wave detectors

Current gravitational wave detectors intended to observe the space-time deformations produced by passing gravitational waves. The general principle is too use an enhanced Michelson interferometer to measure the relative differential length of two orthogonal arms, this differential length should change as one arm is shortened and the other elongated by the passing wave. As a result the output of the interferometer should deviate from its dark fringe working point in the direction of a bright fringe.

The mirrors forming the interferometer are suspended to reduce their seismic motion, large laser power is used to limit shot noise and wide laser beams and high quality materials are employed to work around thermal fluctuations. After proper calibration the obtained data are a time series

$$d(t) = \frac{\Delta L}{L} = F_+(\theta,\phi) h_+(t) + F_\times(\theta,\phi) h_\times(t) + n(t), \tag{5.3}$$

where L is the length of one interferometer arm, ΔL is the arm length difference, $F_+(\theta,\phi)$ and $F_\times(\theta,\phi)$ are geometrical factors taking into account that the interferometer plane and the wave direction of propagation (θ,ϕ) are not orthogonal, and finally $n(t)$ is the sum of various sources of noise. Such an interferometer is the gravitational analogue of a electromagnetic dipole antenna.

This noise $n(t)$ is the largest challenge for gravitational wave detection. It is tackled both by continuous improvements of the interferometers and by refining data analysis techniques. An additional difficulty comes from the presence of numerous spurious transients (called *glitches*), which cause the noise to be highly non-Gaussian and poorly modeled. As a result at least two detectors are needed for a confident detection.

A network of such interferometeric detectors has been constructed and operated in the last decade, the most sensitive detectors being located in the state of Washington and Louisiana in the USA operated by the LIGO collaboration, and in Italy operated by the Virgo collaboration. Given that the signal is common for all these detectors, observational data are shared and analyzed in common.

5.3 Gamma-ray bursts

Gamma-ray burst (GRB) have been first discovered in the early 70's and observed by various satellites since then. As their name imply they are short (at most a few hundred seconds) outbursts of gamma-rays. They are observationally classified by their duration into short GRBs (<2 sec) and long GRBs (>2 sec), but this duration limit does not completely separate the two populations.

Each type of GRBs is thought to be created by a different family of progenitors. The main model for generating a short GRB is the coalescence of a neutron star with another neutron star or a black hole; whereas for long GRBs the model is the collapse of massive rapidly rotating star. In both cases a relativistic jet is launched which produces gamma-rays along its axis. In both cases a large amount of matter at nuclear densities moving at relativistic speed is involved, the perfect condition for producing gravitational waves.

5.4 Data analysis

We will focus here on gravitational wave data analysis techniques for cases where no reliable gravitational waveform is predicted, e.g. for stellar collapse. The general principle is to look for the same signal in a network of detectors.

To simplify the discussion, let us forget about the question of two polarizations and geometrical factors and assume that the observed data in two detectors is respectively

$$d_1(t) = h(t) + n_1(t),$$
$$d_2(t) = h(t) + n_2(t).$$

In that case it is reasonable to consider the two linear combinations

$$d_{\rm diff} = d_1(t) - d_2(t) = n_1(t) - n_2(t),$$
$$d_{\rm sum} = d_1(t) + d_2(t) = 2h(t) + n_1(t) + n_2(t),$$

which subtract and sum the signal $h(t)$. Prior to forming the linear combinations the two time series need to be shifted in time to account for the gravitational wave time of flight between the two detectors which is $\lesssim 30$ ms.

The purpose of $d_{\rm sum}$ is to increase the signal to noise ratio as the signal amplitude is multiplied by 2 and the noise terms are added in quadrature (factor $\sqrt{2}$ for two equally sensitive detectors). Whereas for $d_{\rm diff}$ the signal is subtracted and only detector noise is left, up to cancelling errors $\sim 10\%$ due to the imperfect calibration of each detector. Hence this combination can be used to veto spurious glitches as they will not cancel out between detectors. An illustration of this principle is shown on figure 5.1.

In order to detect transients in these coherent combinations $d_{\rm sum}$ and $d_{\rm diff}$, they are analyzed by decompo-

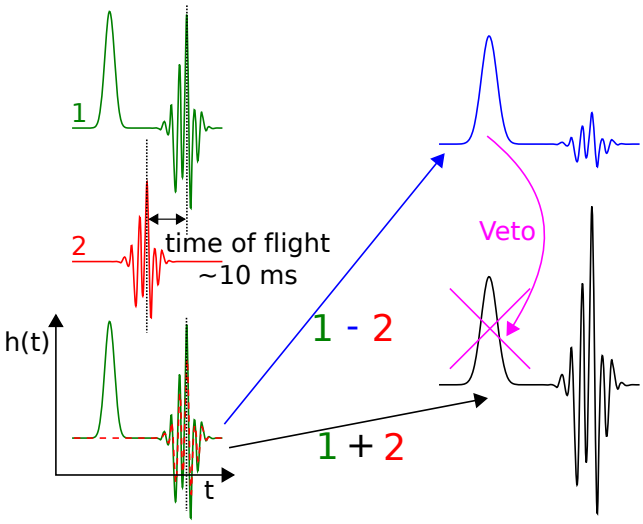


FIGURE 5.1 – Sketch of the principle of data analysis for a gravitational detector network. The data streams (upper left) from two detectors 1 and 2 contain a gravitational signal, and the data stream 1 contains also a glitch. After aligning the two streams in time to account for gravitational wave flight (lower left), the stream difference (upper right) and sum (lower right) are formed. The glitch has a comparable amplitude in both combinations and the difference stream can be used as a veto, the gravitational wave is strongly suppressed (not perfectly due to calibration errors) in the difference stream and is not rejected.

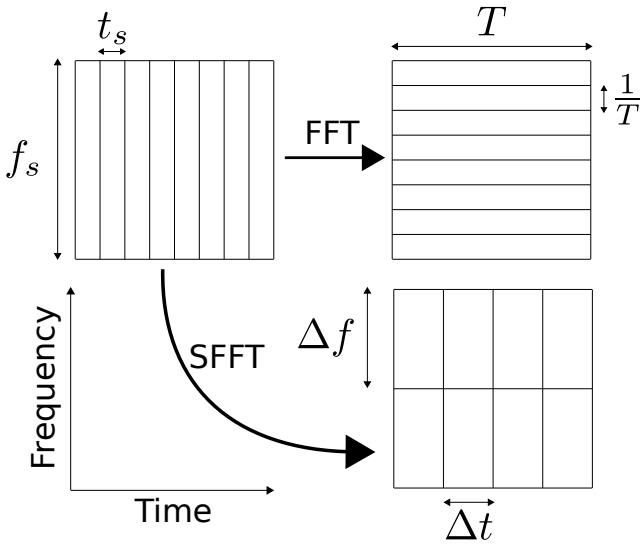


FIGURE 5.2 – Illustration of a time-frequency decomposition. An initial time series (upper left) sampled at a frequency $f_s = 1/t_s$ can be Fourier transformed (FFT) over its whole length T (upper right), but it can also be Fourier transformed in short blocks (SFFT) which are $\Delta t = 1/\Delta f$ long (lower right). This forms a rectangular map of *pixels* and the square of the magnitude of each pixel is called its *brightness*. This time-frequency map of brightness shows the time evolution of the signal power in different frequency bands.

sing them in a time-frequency domain (see figure 5.2) and bright time-frequency pixels are clustered to form candidate events.

In particular when searching for gravitational wave associated with GRBs the electromagnetic trigger provides both a time and sky location information. The sky location reduces the parameter space and simplifies the analysis (among others by giving the exact time of flight delays between detectors), whereas the time reduce the amount of data (and hence noise) analyzed from a few months to a few minutes. When taking into account both effects an order factor 2 in sensitivity is obtained compared to a whole sky all-time analysis.

5.5 Results

In 2005-2007 the LIGO-Virgo network of gravitational wave detectors was operated. During that time $\sim$ 100 GRBs have been observed by γ-ray satellites, mainly Swift. No gravitational wave candidate has been observed for any of these GRBs. Assuming an isotropic energy emission of $0.01\,M_{\odot}c^2$ in gravitational waves, lower limits on the distance to each of these GRBs have been set [2] (see figure 5.3).

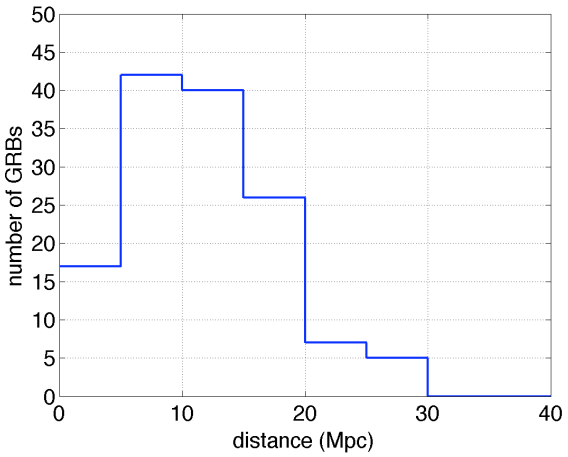


FIGURE 5.3 – Histogram of lower limits on the distance for the set of GRBs observed by the LIGO-Virgo network in 2005-2007.

The typical exclusion distance $\sim 15\,$Mpc is in agreement with the distance distribution for the fraction of GRBs with measured redshifts. Within that distance the expected rate of GRB progenitors is $10^{-6}\,\mathrm{yr}^{-1}$ if all GRBs are considered, and $10^{-3}\,\mathrm{yr}^{-1}$ if the existence of a proposed population of sub-luminous local GRBs is true.

Despite this low expected rates some interesting astrophysical conclusion have been drawn from these observations for one particular GRB. In February 1 2007 a short GRB occurred with a reconstructed sky location error box overlapping with the nearby Andromeda galaxy ($\sim 770\,$kpc). The lack of gravitational wave candidate excludes the binary coalescence model with a confidence level above 99% [3], leaving as possibilities a binary coalescence in a galaxy behind Andromeda or a first observation of an extra-galactic short gamma-ray repeater (star quake on a neutron star).

In conclusion, searching for gravitational waves associated with gamma-ray bursts allows to astrophysically interpret non-observation results, and improves significantly the observational sensitivity which could prove crucial for a first gravitational wave detection. Current experiments are on the verge of gravitational wave observation and the next upgrade planned for 2010-2015 should improve the sensitivity by a factor 10. This translates into a 1000 times larger observational volume, which should be sufficient for regular gravitational wave detections ($\sim$ once per month).

Références

[1] A. Hulse and J. Taylor. Discovery of a pulsar in a binary system. *Astrophys. J. Lett.*, 195, 1975.

[2] B. P. Abbott et al. Search for gravitational-wave bursts associated with gamma-ray bursts using data from LIGO Science Run 5 and Virgo Science Run 1. *Astrophys. J.*, 715 :1438, 2010.

[3] B. P. Abbott et al. Implications for the origin of GRB 070201 from LIGO observations. *Astrophys. J*, 681 :1419, 2008.



Indirect Search for Dark Matter with the ANTARES Neutrino Telescope

Charif, Ziad
Centre de Physique des Particules de Marseille

Résumé

Detecting Dark Matter induced neutrinos via Neutrino telescopes is a realistic goal. Using the data acquired by the ANTARES neutrino telescope in 2008, search for neutrino fluxes produced by Dark Matter auto-annihilation inside the Sun can be performed for various models of Dark Matter.

6.1 Introduction

Dark Matter is a type of Matter that is inferred to exist from a collection of effects and observations of the Universe. Most importantly, it is undetectable by standard telescope as it does not emit or scatter electromagnetic radiation. Its existence is theorized to be responsible for discrepancies between measurements of visible mass and total mass of galaxies, clusters of galaxies and the entire Universe. However if one takes certain assumptions about Dark Matter, it become possible to detect it via other means than electromagnetic signatures. One of them is the possibility of neutrino emissions via Dark Matter auto-annihilation. Hence the role of the ANTARES neutrino telescope[1] comes into play.

6.2 Dark Matter

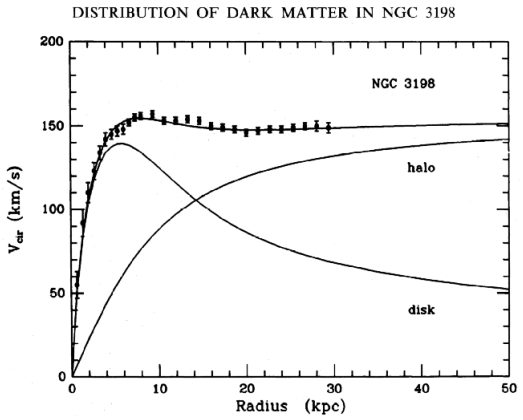


FIGURE 6.1 – Comparison between the actual measured rotation speed curve of NGC3198 galaxy[2], the theoretical rotation curve based on the visible mass of the galaxy, and the theoretical rotation curve with the addition of a halo of matter along the observed matter.

The evidence for Dark Matter mostly comes from astrophysics, we present some of them :

- Galactic rotation curves (Figure 6.1). Taking into account distributions of the stars, nebulas, and other astrophysical objects inside a galaxy, the rotation speed of the galactic disk should slow down as we move away from the center of the galaxy. However as different measurements showed, this is not the case, as it actually grows to a constant, indicating the existence of some invisible halo of matter, who's density increases with distance.
- CMB or Comsic Microwave Background. The measurements of the CMB anisotropy done by WMAP[3] experiment was the key role in establishing the ΛCDM model, which is the standard model of cosmology. This model necessitates the existence of Dark Matter and Dark Energy in order to explain the temporal evolution of the Universe on a large and a small scale.
- Gravitational lensing. As predicted by General Relativity, gravitational fields can bend and alter the trajectories of light passing nearby. This effect can be predicted and calculated based on the size, and mass of the object. However as measurements were done for galaxies, differences were found between observed mass and mass calculated from the observed gravitational lensing of these objects, indicating the existence of some invisible mass.

Following the ΛCDM model, Dark Matter is a relic particle from the Big Bang. Hence with the use of Boltzmann equation, one can have an accurate prediction of the relic density of Dark Matter in the Universe today, which is roughly $\Omega_{DarkMatter} \approx \frac{10^{-26} cm^3 s^{-1}}{<\sigma v>}$. Since $\Omega_{Universe} \approx 1$, the thermally averaged annihilation cross section of two Dark Matter particles $<\sigma v>$ is exactly what is predicted for particles at the ElectroWeak scale. Since there are many problems with the Standard Model of particle physics, which can be solved by the introduction of new physics at the Electroweak scale, it is then very tempting to look for new physics models that have a Dark Matter particle candidate. Those new massive particles should interact only via the Weak force (WIMP), since Dark Matter particles should be electrically neutral. Many studied new physics models generate such particle. We list the two most popular Dark Matter candidates :

1. Lightest Supersymmetric Particle (LSP) in Supersymmetry (SUSY). In one particular extension of the Standard Model of particle physics, Supersymmetry, each particle of the Standard Model has a

partner particle introduced by Supersymmetry. In many cases of SUSY parameter space, the lightest superpartner (LSP) is a stable partcile with no electrical charge and is thus a perfect candidate for Dark Matter.

2. Lightest Kaluza-Klein Particle (LKP) in Unified Extra Dimensions (UED) models. In UED, which is another extension of the Standard Model of particle physics, there is an introduction of one or more extra small spatial dimensions, depending on the specific model used. Some of these models predict a stable neutral massive particle that interacts mainly via the Weak interaction, and can be considered as a Dark Matter candidate.

Since the ΛCDM model also require the Dark Matter to be thermally cold, this allows them to be gravitationally caught by massive objects, such as planets, stars, galaxies, and clusters. So with the assumption that Dark Matter can be explained by LSP or LKP, these two models give the possibility of Dark Matter candidates to auto-annihilate, giving neutrinos at the end process. This is why it is very tempting to search for Dark Matter via its neutrino signal.

6.3 The ANTARES Neutrino Telescope

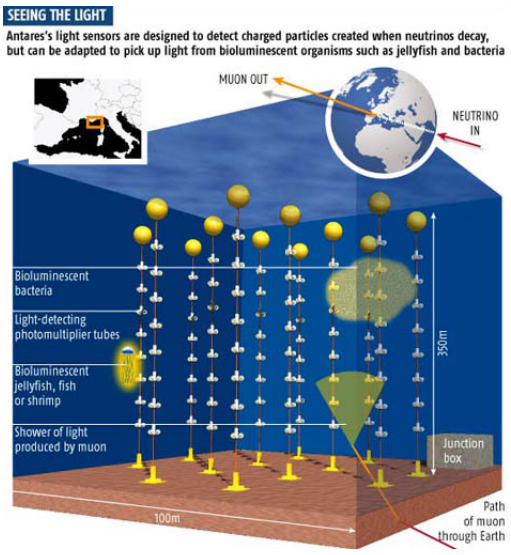


FIGURE 6.2 – Scheme of the ANTARES detector

The ANTARES neutrino telescope is one of three similar detectors in the world, and the first in sea water. The construction of ANTARES was finished in 2008 with the deployment of its 12th line. It is located 40 km offshore of Toulon in the Mediterranean sea, at a depth of 2500m. It consists of 12 lines, 25 floors per line, with 3 Optical Modules (Figure 6.3) per floor, resulting in a three dimensional distribution of 900 OMs in the entire detector (Figure 6.2). The main goal of the experiment is to look for the Cherenkov light emitted by high energy muons during their travel in the sea



FIGURE 6.3 – Example of one Optical Module used in ANTARES

water throughout the detector. The trajectory of the muon track is reconstructed from the detection of the timing of the Cherenkov photons as well from the positions of the photodetectors. An indirect searc for neutrinos can then be performed by selecting the upward going muons produced by neutrinos which have passed trough the entire planet and interacted in the vicinity of the detector. The direction of the incoming neutrino, being almost collinear with the seconday muon, can then be determined with an accuracy reaching 0.2° for high energy neutrinos above 10TeV. The ANTARES detector has a lower energy threshold about 20 GeV for reconstructed neutrinos and thus suitable for the search of Dark Matter induced neutrino signals.

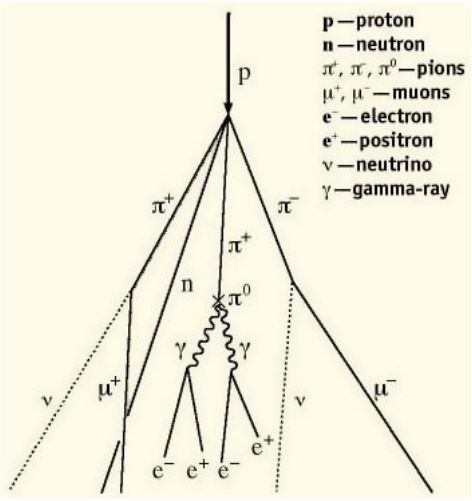


FIGURE 6.4 – The creation process of muons, and neutrinos from Cosmic Rays hitting earth's atmosphere.

The main background is due to down-going muons coming from cosmic rays interaction above the detector with the atmosphere, a large fraction being removed by selecting up-going muons. Another irreducible background comes from up-going muons generated by atmospheric neutrinos also coming from Cosmic Rays interaction with the atmosphere (Figure 6.4) but from the other side of the Earth. In addition there is some electromagnatic noise coming from bioluminescence acitivty produced by bacteria and sea life, as well as from K40 radioactivity. Its main effect is to degrade

the quality of the muon reconstruction. For example some down-going muons can be reconstructed as up-going due to the addition of extra hits recorded on some OMs.

6.4 Indirect search of Dark Matter with ANTARES

Search for Dark Matter is divided into two main strategies, direct detection looking for energy deposition due to Dark Matter interaction with a detector. The other strategy is indirect search, looking for secondary particles emitted by Dark Matter auto-annihilation in space. This opens up the possibility of searching for Dark Matter via its neutrino signal. Multiple different cosmic sources can be investigated with ANTARES : Sun, Earth Center, Galactic Center, Galactic Halo, and Dwarf Galaxies.

6.4.1 Analysis towards the Sun

The Sun offers a great opportunity to test the hypothesis as previously proposed. Its large gravitational well and close distance to Earth can produce Dark Matter neutrino fluxes that are large enough to be detected.

In order to calculate the detector sensitivity to different models of Dark Matter in comparision with background, we use a monte carlo production of signal as well as of atmospheric neutrinos and atmospheric muons. The Dark Matter neutrino flux signals have been obtained via simulation with WIMPSIM[4]. This code simulates neutrino spectrum produced by Dark Matter auto-annhilation inside the Sun, the different interactions of neutrinos and anti-neutrinos with the Sun matter, and the neutrino oscillations during their travels towards Earth. To probe different models, different masses of Dark Matter particles were simulated, as well as different annihilation channels which can lead to extreme cases of hard and soft neutrino spectrums. The softest flux is due to $\chi\bar{\chi} \rightarrow b\bar{b}$. The hard flux has been studied with two different channels. In most general models the hardest flux is produced by $\chi\bar{\chi} \rightarrow \tau^+\tau^-$. However to study SUSY models it is commun to use fluxes produced by $\chi\bar{\chi} \rightarrow W^+W^-$ since the branching ratio to $\tau^+\tau^-$ is usually suppressed in comparison with W^+W^- in such models.

Figure 6.5 represents the distribution of Tchi2, the quality of track reconstruction in the hypothesis of a muon generating a Cherenkov cone. This variable helps to differentiate between up-going neutrino induced muons, badly reconstructed down-going Cosmic Rays induced muons, and muons produced by Dark Matter neutrinos. A good agreement between Data recorded by the ANTARES detector in 2008 and simulated backgrounds can be seen. Figure 6.6 shows the distribution of the number of events inside a cone centered around the Sun during data acquisition period, as function of the half-cone openning angle. This variable helps in differentiating between our atmopsheric neutrino background, and Dark Matter neutrino signal.

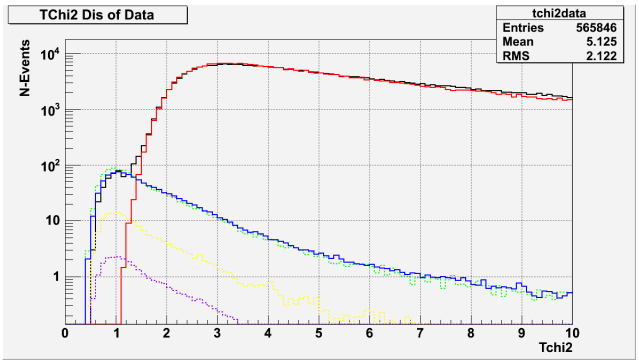


FIGURE 6.5 – Distribution of the track quality parameter for **Data**, **Atmospheric Muon Monte Carlo**, **Atmospheric Neutrino Monte Carlo**, and neutrino signal from different Dark Matter models.

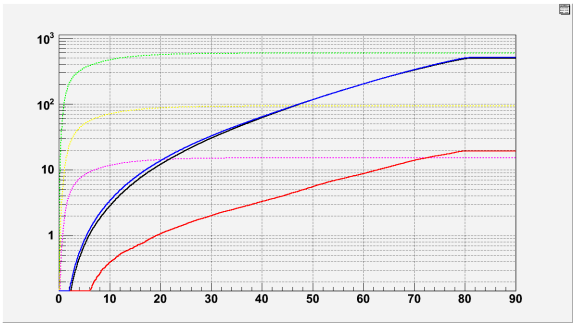


FIGURE 6.6 – Distribution of number of events inside a cone centered around the Sun as function of the half-cone openning angle in degrees for **Data**, **Atmospheric Muon Monte Carlo**, **Atmospheric Neutrino Monte Carlo**, and neutrino signal from different Dark Matter models.

To optimize the analysis for best sensitivity to Dark Matter neutrinos with respect to background, the Feldman-Cousin method[5] has been used on two variables, which are tchi2 and the half-cone angle for each chosen model of Dark Matter. This background was also estimated using the Data set itself, this was done by creating a fake direction of the Sun for each event by changing its recording time. Figure 6.7 presents an example of this minimization. After applying a given cut on Tchi2, the blue curve represents the fluctuation of the background with a 90%CL. This curve represents the upper limit of the statistical fluctuations of the Data sample in the absence of any detected Dark Matter signal. In addtition, the red curve represent the output of the Feldman-Cousin minimization for the signal, its minimum being the half-cone optimal cut value. The sensitivity is given by the lowest neutrino flux obtained via the optimization procedure over all the tchi2 and half-cone angle parameter space.

Figure 6.8 shows the minimal Dark Matter neutrino fluxes detectable by analysing the ANTARES Data recorded during 2008, as a function of the Dark Matter particle mass for the soft and hard spectrum models.

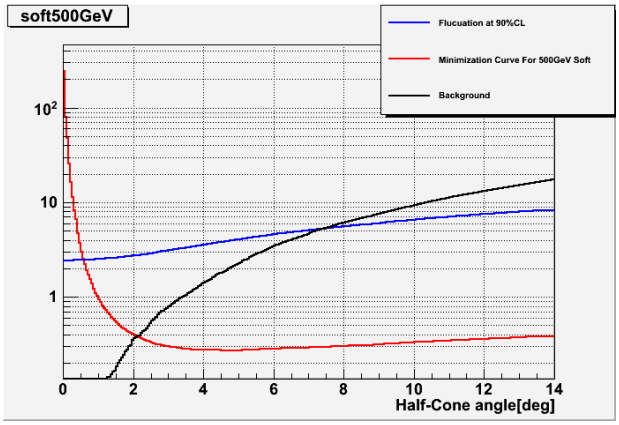


FIGURE 6.7 – Distribution of number of **Data** events inside a cone centered around the Sun as function of the half-cone openning angle, **Minimization curve of Feldman-Cousin for a model of Dark Matter** as a function of the half-cone openning angle, and **fluctuations at 90%CL of the background**

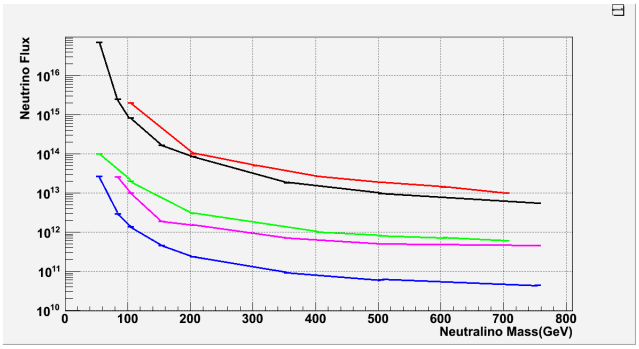


FIGURE 6.8 – Minimal detectable Dark Matter neutrino flux as a function of the Dark Matter mass. 2007 Data - soft flux, **2008 Data - soft flux**, 2007 Data - hard fluxes W^+W^-, 2008 Data - hard fluxes W^+W^-, 2008 Data - hard fluxes $\tau^+\tau^-$

6.5 Conclusions

The ANTARES detector which was completed in 2008, is the first under sea neutrino telescope and the largest one in the Northern hemisphere. The neutrino sample detected by ANTARES in 2008 is currently analysed to look for Dark Matter annihilation signal towards the direction of the Sun. The analysis presented is very robust and simple, and presentes an interesting sensitivity to a class of Dark Matter models. Using the method presented here, the results of the analysis of 2007-2008 combined Data set is expected soon. Projected results show the ability to probe some interesting SUSY Dark Matter models (Figure 6.9) with only three years of ANTARES Data. Moreover, this analysis can be improved via an implementation of a dedicated low energy reconstruction algorithm, an implementation of an energy estimator as well as the use of a multivariate technique instead of this simple method based on sequential cuts. The advantage of this directional search is that it can be easily adapted for use on other sources, such as the galactic center and Dwarf galaxies.

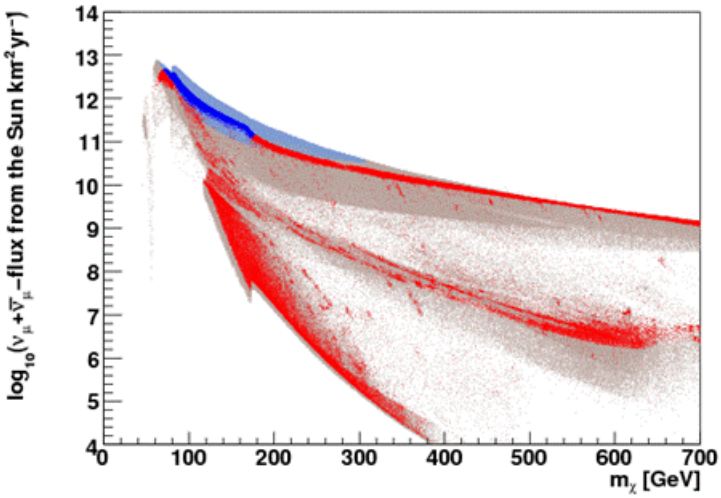


FIGURE 6.9 – Sensivity of ANTARES to neutrinos produced by annihilation of Dark Matter into the Sun in a class of SUSY models (CMSSM) which can be obtained with 3 full years of lifetime with the 12 lines detector. **90%CL excludable by ANTARES (models with relic density within 2σ of the WMAP region)**, 90%CL excludable by ANTARES(Models with relic density outside the 2σ WMAP region), Other models are not excludable by ANTARES

Références

[1] A. Aguilar et al. (ANTARES Collaboration), "ANTARES, the first operational neutrino telescope in the Mediterranian Sea", to be published in *Nuclear Instruments & Methods*.

[2] T. S. van Albada et al., *Astrophys. J.* **295**, 305 (1985).

[3] J. Dunkley et al., *Astrophys. J. Suppl.* **180**, 306 (2009).

[4] M. Blennow, J. Edsjö and T. Ohlsson, [arXiv : 0709.3898]

[5] G.L. Feldman and R.D. Cousins, *Phys. Rev. D* **57**, 3873 (1998).

Estimation de rayon de courbure des gerbes atmosphériques par la méthode de radiodétection avec CODALEMA

A. Rebai
SUBATECH, IN2P3-CNRS, Université de Nantes, Ecole des Mines de Nantes

Résumé

La détection des transitoires radio associés aux grandes gerbes atmosphériques constitue une méthode nouvelle de mesure des rayons cosmiques d'ultra haute énergie (UHECR). Aprés une bréve description de l'expérience de radiodétection CODALEMA, une méthode de calcul des rayons de courbure des fronts d'onde radio est présentée. Les performances de cette méthode d'estimation appliquée à des données simulées et à des données collectées par CODALEMA sont discutées.

7.1 Introduction

Malgré les efforts expérimentaux intenses au cours des 20 derniéres années, l'origine et la nature des rayons cosmiques d'ultra haute énergie (>PeV) restent encore mal comprises. Les incertitudes sont liées pour partie au flux extrêmement faible de rayonnement (1 particule/siécle/km^2 à 10^{20} eV) mais aussi aux erreurs expérimentales systématiques inhérentes aux différentes techniques de détection utilisées [1]. L'une des améliorations possibles des mesures pourrait être donnée par l'exploitation des signaux radioélectriques produits par le mouvement des particules secondaires dans la gerbe atmosphériques. Cette méthode de détection, qui se trouve à mi chemin entre les techniques utilisées en physique des particules et en radioastronomie, a été proposée par Askaryan en 1962 [2] et étudiée jusqu'à la fin des années 60, puis abondonnée en raison des difficultés d'interprétations des résultats expérimentaux [3]. La nécessité de détecteurs plus performants [4], la sensibilité au développement longitudinal de la gerbe, le cycle utile proche de 100%, le coût faible des capteurs, ont rendu cette alternative de détection attractive avec les technologies actuellement disponibles. Cette activité a été relancée au début des années 2000 notamment par la collaboration CODALEMA [5] en France et LOPES [6] en Allemagne.
Depuis 2002, l'expérience de radiodétection, CODALEMA [7], hébergée sur le site de l'observatoire de Nançay, vise à étudier l'ensemble des potentialités de cette détection dans la gamme d'énergie de 10^{16} eV (seuil de détection) à 10^{18} eV (limite supérieure imposée par la surface instrumentée). Elle est constituée d'un réseau de 17 détecteurs de particules, du réseau décamétrique DAM, ainsi que d'un réseau de 24 antennes dipoles actifs réparties sur une surface d'environ 1/4 km^2 (figure 7.1). Le déclenchement de l'ensemble du système d'acquisition des données est défini par le

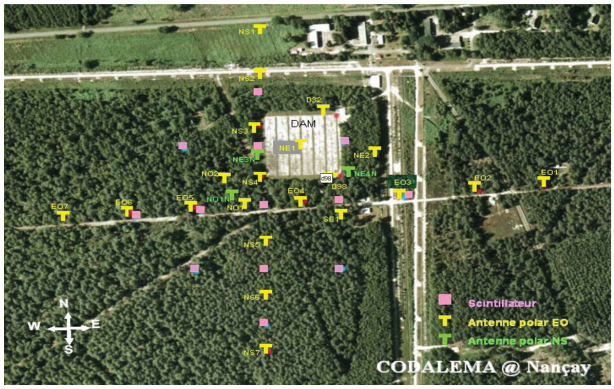


FIGURE 7.1 – Set up de l'expérience CODALEMA montrant la disposition du réseau des détecteurs de particule (rouge) et du réseau d'antennes (jaune) utilisés pour cette étude.

passage en coîncidence de particules au travers de chacun des 5 détecteurs de particules centraux. Ce trigger particule définit un seuil de détection en énergie des gerbes d'environ 5.10^{15} eV. La forme d'onde radio de chaque antenne est enregistrée dans une bande de fréquence 0-250 MHz durant une fenêtre temporel de 2.5 μs avec une fréquence d'échantillonnage de 1GS/s. Les événements radio, candidats de gerbes atmosphériques (contrepartie de la gerbe vue par les détecteurs de particules), sont identifiés durant l'analyse offline [7] [8]. À l'issue de cette étape d'analyse, un jeu de données comportant les paramètres de la gerbe reconstruite à l'aide des informations fournies par les détecteurs de particules (temps d'arrivée, direction d'arrivée, position du pied de gerbe, énergie) ainsi qu'un ensemble d'observables radio pour chaque antennes (temps d'arrivée, amplitude du signal radio) ainsi que les observables de la gerbe reconstruite par l'exploitation des données radio seules (temps d'arrivée, direction d'arrivée, position du pied de gerbe, énergie) sont obtenus événement par événement. Ces observables sont utilisées pour étudier la courbure du front de l'onde radio qui pourrait constituer l'une des variables discriminantes de la nature du primaire (estimation du X_{max}).

7.2 Principe de la reconstruction du centre d'émission radio

Ce travail repose sur l'hypothèse que le centre d'émission est situé sur la droite définie par la position du pied de gerbe et la direction d'arrivée de l'onde (assi-

milée à un plan). Ces quantités sont fournies par l'analyse offline [7]. La direction d'arrivé de l'onde (d'angles zénithal θ et azimutal ϕ) est déterminée par l'analyse des temps d'arrivées t_i du transitoire radio sur chaque antenne de position (x_i, y_i, $z_i = 0$). Le vecteur du plan d'onde résultant a pour composantes : $u = cos(\phi).sin(\theta)$, $v = sin(\phi).sin(\theta)$. La position du pied de gerbe (x_c, y_c, $z_c = 0$) est déduite de l'analyse du profil latétral du champ électrique.
L'équation du front d'onde sphérique émis à partir du centre d'émission de coordonnées (x_0, y_0, z_0) s'écrit :

$$(x - x_0)^2 + (y - y_0)^2 + (z - z_0)^2 = R^2$$

Les coordonnées du centre d'émission (x_0, y_0, z_0) qui se trouve sur la droite définie par (θ, ϕ, x_c, y_c) peuvent s'exprimer par les relations suivantes :

$$x_0 = R.u + x_c$$
$$y_0 = R.v + y_c$$
$$z_0 = R.cos(\theta)$$

Avec $R = c.(t - t_0)$, la distance parcourue au temps t par l'onde qui se propage à la vitesse la lumière et produite à l'instant initial d'émission t_0. Les coordonnées du centre d'émission sont obtenues en utilisant la méthode des moindres carrés construites à partir de la fonction à 4 inconnues :

$$\chi^2 = \sum_{i=1}^{multiplicit} ((x_i - x_0)^2 + (y_i - y_0)^2 + (z_i - z_0)^2 - c^2.(t_i - t_0)^2)^2$$

En écrivant les coordonnées du centre d'émission recherché en fonction des deux seules inconnues R et t_0, l'équation peut se refomuler sous la forme :

$$\chi^2 = \sum_{i=1}^{multiplicit} ((x_i - R.u - x_c)^2 + (y_i - R.v - y_c)^2$$
$$+(z_i - R.cos(\theta))^2 - c^2.(t_i - t_0)^2)^2$$

Du fait du terme non-linéaire de χ^2, il n'est pas possible de déterminer le minimum par une méthode analytique et une méthode de résolution numérique doit être utilisée (*Matlab Optimization Toolbox*).

7.3 Résultat de reconstruction du centre d'émission radio

La méthode de résolution numérique a été testée en utilisant un jeu de valeurs d'essais. Pour ce faire, différentes positions du centre d'émission peuvent être introduites et les temps d'arrivées sur les antennes sont obtenus en calculant les temps de propagation de l'onde sphérique et en tenant compte de la géométrie du réseau. Les erreurs expérimentales sur les temps détectés sont ajoutées par tirages Monte Carlo de distributions gaussiennes d'écart type choisis (entre 0 et 15 ns). La figure 7.2 montre un résultat de la reconstruction sphérique sur des simulations pour un rayon de courbure égal à 15 km et des erreurs temporelles égales à $0ns$, $1ns$, $2ns$ ou $10ns$. Afin de prendre en compte de la géométrie particulière en croix du réseau, la position en angle zénithale du point d'émission a été fixée mais l'angle azimutal est variable. Les résultats montrent que les erreurs en temps sur les antennes constituent le facteur le plus limitant pour l'estimation du rayon de courbure.
Dans une deuxiéme étape, les résultats de la minimisation ont été analysés et comparés à ceux obtenus avec des données réelles. Pour exemple, trois fonctions du χ^2 sont présentées figure 7.3, l'une pour des données simulées et les deux autres pour des données réelles. Il ressort que concernant les données expérimentales, le minimum global peut être difficile à localiser précisément et qu'en conséquence l'estimation du rayon de courbure sera moins robuste. Finalement, un sous ensemble des événements gerbe de l'expérience CODALEMA étiquetés événements centraux [9] a été utilisé pour estimer les rayons de courbure. Pour ces événements. l'ensemble des observables de la gerbe (direction d'arrivée, pied de gerbe, énergie) est parfaitement caractérisé à la fois pour le réseau de détecteur de particules et pour le réseau radio. La figure 7.4 montre la distribution des rayons de courbure obtenue pour ces évnéments. Le résultat est inattendu et diffère de celui obtenu en utilisant une méthode d'estimation diffèrente [10]. De plus car compte tenu de la valeur la plus vraisemblable de la distribution, il ne semble pas que ce soit le maximum de la gerbe qui soit observé. Ce résultat peut être la conséquence d'une mauvaise estimation du temps sur les antennes ou bien d'une évaluation erronée de l'erreur estimée sur la mesure temporelle. A titre d'essai, la variation du rayon de courbure moyen a été tracée en fonction de l'angle zénithal (figure 7.5). Il semble que la variation avec l'angle suive mieux

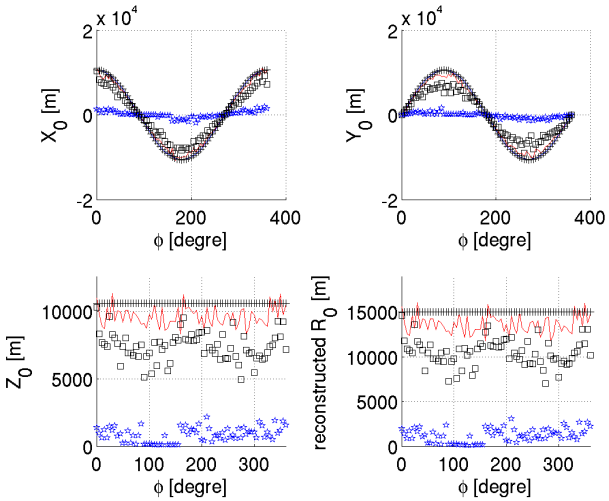


FIGURE 7.2 – Reconstruction du centre d'émission fixé à R=15 km pour $\theta = 45$ et ϕ variant entre 0° et 360° pour des temps exacts d'arrivées sur les antennes (en croix noires) et pour des erreurs temporelles de 1 ns (trait continu rouge) et 2 ns (carrés noirs) et 10 ns (étoiles bleues).

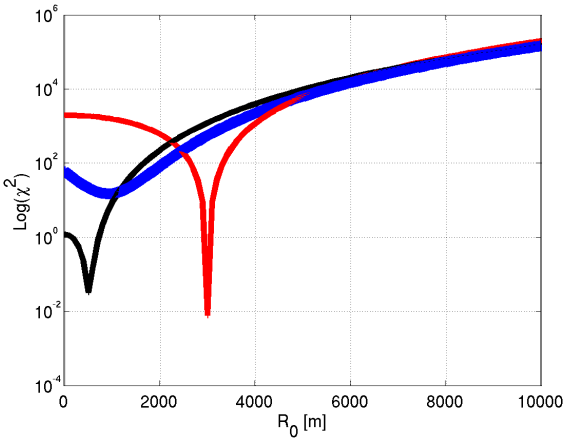


FIGURE 7.3 – Fonctions de χ^2 obtenues pour un événement réel (courbe noire) et un événement similaire simulé avec un centre d'émission à 3 km sur la même direction d'arrivée (courbe rouge). La courbe bleue présente un autre événement réel suggérant que la localisation du minimum peut être plus difficile.

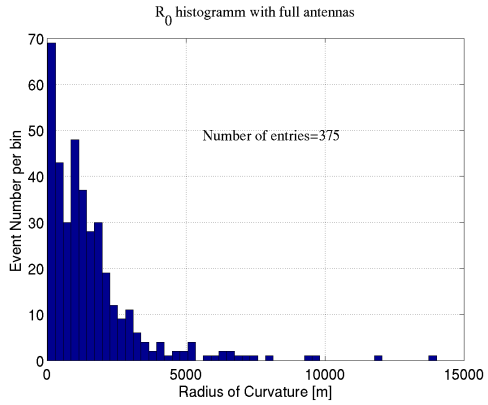


FIGURE 7.4 – Histogramme des rayons de courbures

l'évolution attendue en indiquant une augmentation de R avec l'angle car le maximum de la gerbe s'éloigne de l'observateur.

7.4 Conclusion

Une méthode de reconstruction du rayon de courbure associé à l'onde radio produit par le développement des gerbes atmosphériques initiées par les UHECR a été présentée. Les simulations indiquent (que pour des rayons inférieurs à 15 km et des erreurs temporelles inférieures à 5 ns) la méthode fournit des estimations correctes du rayon de courbure, mais que les résultats dérivés de l'exploitation des données expérimentales restent mal compris.

Ce travail a bénéficié d'un financement de la région Pays de la Loire.

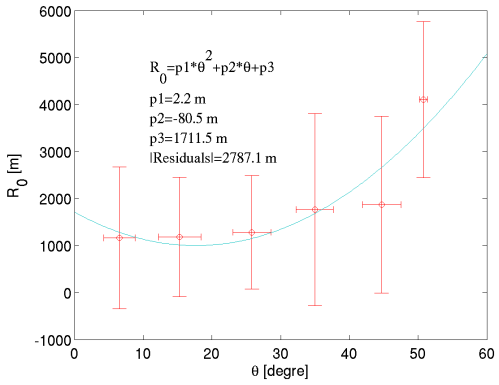


FIGURE 7.5 – Corrélation entre le rayon de courbure et l'angle zénithal θ

Références

[1] *Pierre Auger Collaboration, Astropart. Phys. 31 (2009) 399, Pierre Auger Collaboration, Phys. Rev. D 79 (2009) 102001, Pierre Auger Collaboration, Astropart. Phys. 29 (2008) 188, The High Resolution Fly's Eye Collaboration, Phys. Lett. B 619 (2005) 271, Pierre Auger Collaboration ICRC 09, arXiv :0906.2347 [astro-ph], Pierre Auger Collaboration ICRC 09, arXiv :0906.2319 [astro-ph], M. Lemoine et E. Waxman, JCAP 0911 :009 (2009).*

[2] G. Askaryan *J Exp Theor Phys*, vol. 21, p. 658, 1962.

[3] H. Allan *Progress in Elementary Particle and Cosmic Ray Physics*, vol. X, p. III, 1971.

[4] D. Fegan, "Arena 2010 conference, nantes," *Nucl.Instrum.Meth A*, 2011.

[5] D. Ardouin *al Nucl.Instrum.Meth A*, vol. 555, p. 148, 2005.

[6] H. Falcke *al Nature*, vol. 435, p. 313, 2005.

[7] D. Ardouin *al Astroparticle Phys*, vol. 26, pp. 341–350, 2006.

[8] D. Ardouin *al Astroparticle Phys*, vol. 31, pp. 192–200, 2009.

[9] O. Ravel, "Arena 2010 conference, nantes," *Nucl.Instrum.Meth A*, 2011.

[10] C. Rivière, "thèse de l'université de joseph fourrier," 2009.